ERDC/CRREL TR-19-16

Cold Regions Research and Engineering Laboratory

US Army Corps of Engineers®
Engineer Research and Development Center

ERDC
ENGINEER RESEARCH & DEVELOPMENT CENTER

ERDC 6.2 Geospatial Research and Engineering (GRE) ARTEMIS STO-R

Macroscale Salt-Crust Formation on Indoor Playa-Like Test Plots for Dust-Emission Research Applications

Methodology Assessment

Matthew F. Bigl, Sandra L. LeGrand, Samuel A. Beal, Ariana Sopher, and David B. Ringelberg

August 2019

The U.S. Army Engineer Research and Development Center (ERDC) solves the nation's toughest engineering and environmental challenges. ERDC develops innovative solutions in civil and military engineering, geospatial sciences, water resources, and environmental sciences for the Army, the Department of Defense, civilian agencies, and our nation's public good. Find out more at www.erdc.usace.army.mil.

To search for other technical reports published by ERDC, visit the ERDC online library at http://acwc.sdp.sirsi.net/client/default.

ERDC/CRREL TR-19-16
August 2019

Macroscale Salt-Crust Formation on Indoor Playa-Like Test Plots for Dust-Emission Research Applications

Methodology Assessment

Matthew F. Bigl, Sandra L. LeGrand, Samuel A. Beal, Ariana Sopher, and David B. Ringelberg

U.S. Army Engineer Research and Development Center (ERDC)
Cold Regions Research and Engineering Laboratory (CRREL)
72 Lyme Road
Hanover, NH 03755-1290

Final Report

Prepared for Assistant Secretary of the Army for Acquisition, Logistics, and Technology
103 Army Pentagon
Washington, DC 20314-1000

Under ERDC 6.2 Geospatial Research and Engineering (GRE) Army Terrestrial-Environmental Modeling and Intelligence System Science Technology Objective–Research (ARTEMIS STO-R) under WIC 4433FB/U4357514, "Dynamic Undisturbed Soils Testbed to Characterize Local Origins and Uncertainties of Dust (DUST-CLOUD)"

Abstract

Playas (dry lakebeds), which are often used as stable surfaces for landing zones and ground maneuver, can also be prolific sources of dust. Accurate prediction of playa susceptibility to dust emission is essential for military operations in arid regions. The goal of this study was to determine if methodologies originally developed for bench-scale laboratory analyses of surficial salt-crust features common to playas could also be used to create macroscale samples for dust-related research applications in a large-scale indoor testing facility.

Playa salt crust conditions were simulated on six meter-scale plots (2 m × 2 m) and one large-scale plot (7.3 m × 5.5 m) of compacted, well-mixed loamy soil by controlling climatic parameters, the water-delivery mechanism, and surface-soil heating. The resulting simulated-playa surfaces were characterized for developed crust thickness, compressive and shear strength, chemical composition, and dust-emission potential. Resultant crust attributes varied; however, all methods tested developed simulated playas with physical conditions that were comparable to real-world analogues. Although chemical composition was not evaluated in our real-world comparison, we found that our water delivery method had a statistically significant effect on the chemical attributes of the simulated crusts.

Contents

Figures and Tables

Figures

Tables

Preface

This study was conducted for the Assistant Secretary of the Army for Acquisition, Logistics, and Technology under the U.S. Army Engineer Research and Development Center (ERDC) 6.2 Geospatial Research and Engineering (GRE) Applied Research Program's Army Terrestrial-Environmental Modeling and Intelligence System Science Technology Objective—Research (ARTEMIS STO-R), WIC 4433FB/U4357514, "Dynamic Undisturbed Soils Testbed to Characterize Local Origins and Uncertainties of Dust (DUST-CLOUD)." The technical monitor was Mr. John Eylander, ERDC Cold Regions Research and Engineering Laboratory (CRREL).

The work was performed by the Engineering Resources Branch (CEERD-RRE), the Terrestrial and Cryospheric Sciences Branch (CEERD-RRG), the Biogeochemical Sciences Branch (CEERD-RRN), and the Force Projection and Sustainment Branch (CEERD-RRH) of the Research and Engineering Division (CEERD-RR) and the Office of the Technical Directors (CEERD-RZT), ERDC Cold Regions Research and Engineering Laboratory (CRREL). At the time of publication, Dr. Caitlin Callaghan was Acting Chief, CEERD-RRE; Dr. John Weatherly was Chief, CEERD-RRG; Dr. Justin Berman was Chief, CEERD-RRN; Mr. Justin Putnam was Acting Chief, CEERD-RRH; and Mr. Jared Oren was Acting Chief, CEERD-RR. The Deputy Director of ERDC-CRREL was Mr. David B. Ringelberg, and the Director was Dr. Joseph L. Corriveau.

The authors acknowledge the following CRREL employees for experimentation support: Mr. Bruce Elder, Ms. Stacey Doherty, Mr. Keran Claffey, Mr. Andrew Bernier, Mr. Charles Smith, Mr. Chris Williams, Mr. Kyle Elliot, Mr. William Burch, and Mr. Charles Schelewa. The authors would also like to thank Dr. Mark Chappell of the ERDC Environmental Laboratory and Dr. Harland Goldstein of the U.S. Geological Survey for consultation on soil parameters and test design. Mr. Dan R. Glaser and Ms. Emma Ambrogi, CRREL, provided manuscript review comments.

COL Ivan P. Beckman was Commander of ERDC, and Dr. David W. Pittman was the Director.

Acronyms and Abbreviations

ANOVA	Analysis of Variance
ARTEMIS	Army Terrestrial Environmental Modeling and Intelligence System
C	Carbon
Ca	Calcium
Ca^{2+}	Calcium (II) Ion
$CaCl_2$	Calcium Chloride
$CaCl_2 \cdot H_2O$	Calcium Chloride Hydrate
$CaSO_4$	Calcium Sulfate
Cl	Chloride
Cl^-	Chloride Ion
CRREL	Cold Regions Research and Engineering Laboratory
D	Direct
DUST-CLOUD	Dynamic Undisturbed Soils Testbed to Characterize Local Origins and Uncertainties of Dust
EC	Electrical Conductivity
EDS	Energy Dispersive X-Ray Spectroscopy
ERDC	U.S. Army Engineer Research and Development Center
FERF	Frost Effects Research Facility
GH	Greenhouse
GRE	Geospatial Research and Engineering
GW	Groundwater
HL	Heat Lamp
HPS	High-Pressure Sodium

HSD	Honest Significant Difference
I	Indirect
K	Potassium
K^+	Potassium Ion
LS	Large-Scale
LS-E	Large-Scale East
LS-W	Large-Scale West
Mg	Magnesium
Mg^{2+}	Magnesium (II) Ion
$MgSO_4$	Magnesium Sulfate
$MgSO_4{\cdot}7H_2O$	Magnesium Sulfate Heptahydrate (Epsom Salt)
MP	Moisture Probe
MS	Meter-Scale
Na	Sodium
Na^+	Sodium Ion
NaCl	Sodium Chloride
$NaHCO_3$	Sodium Bicarbonate
NO_3^-	Nitrate Ion
O	Oxygen
P	Phosphorus
$PO4^{3-}$	Phosphate Ion
PCA	Principal Component Analysis
PI-SWERL	Portable In Situ Wind Erosion Laboratory
PM10	Particulate Matter of Size 10 µm or Less

rpm	Revolutions Per Minute
RSD	Relative Standard Deviation
S	Sulfur
SEM	Scanning Electron Microscope
Si	Silicon
SM	Misting
SO_4^{2-}	Sulfate Ion
STO-R	Science Technology Objective—Research
T	Temperature
TDS	Total Dissolved Solids
Tr	Thermostat
TR	Temperature/Relative Humidity Probe

Unit Conversion Factors

Multiply	By	To Obtain
cubic feet	0.02831685	cubic meters
degrees Fahrenheit	(F-32)/1.8	degrees Celsius
feet	0.3048	meters
inches	0.0254	meters
miles (U.S. statute)	1,609.347	meters
miles per hour	0.44704	meters per second
pounds (force)	4.448222	newtons
pounds (mass)	0.45359237	kilograms

1 Introduction

1.1 Background

Playas are dry lakebeds, commonly found in arid regions, that can support military operations when used as ad hoc aircraft landing sites and in ingress and egress vehicular ground maneuvers. However, these geomorphic landscape features can also be prolific sources of soil dust (Prospero 2002; Reynolds et al. 2007; Bullard et al. 2016). The physical and chemical characteristics of playa crusts play an integral role in how susceptible the surface is to dust lofting. By understanding the underlying processes that lead to this susceptibility, we gain an operational advantage. Accurate prediction of playa surface susceptibility to dust emission is essential for desert-region mission planning and terrain intelligence applications.

Although field research can greatly enhance our understanding of dust mobilization processes, it can also be time-consuming and costly. Developing a simulated playa surface in an indoor large-scale facility could considerably expedite dust-related research and testing activities. Although exact replication of a playa system in the laboratory is likely unachievable, the ability to recreate key playa surface behaviors, like salt crusting, could be useful in developing dust-lofting forecast models and in developing and evaluating mitigation strategies.

Evaporitic soluble salt-crust formation (i.e., crusts that form when dissolved salts or carbonates infiltrate the soil surface and recrystallize when moisture evaporates) can markedly decrease soil erosion potential (Langston and McKenna-Neuman 2005; Reynolds et al. 2007). Historically, bench-scale salt-crusted soil samples (i.e., samples prepared in petri dishes or shallow pans) have been used for wind-tunnel dust-emission studies (e.g., Langston and McKenna-Neuman 2005; Nield et al. 2016); however, we are unaware of any successful efforts to produce salt-crusted playa-like soil plots large enough for applications like vehicular dust-emission testing.

1.2 Objectives

The goal of this study was to investigate if salt crusts could be formed on indoor, macroscale, playa-like soil plots by using climate control and two distinct saltwater-delivery mechanisms, above and below surface wetting.

Specific research objectives were

1. to assess the effect of two different saltwater-delivery methods on salt-crust formation in a highly controlled environment,
2. to investigate the sensitivity of crust formation to two different salinity concentrations, and
3. to determine if salt-crust formation could be achieved in a similar time frame via either water-delivery method without the use of dehumidification or ambient temperature control.

1.3 Approach

In this study, we used two different saltwater-delivery mechanisms to seed salt-crust formation on simulated playas and evaluated their effectiveness. These brackish water-supply methods included (1) drawing salt solution to the soil surface from an artificial groundwater source through the matric potential of the soil and (2) misting the soil surface with a salt solution (referred to henceforth as the groundwater and misting approaches, respectively). Both methods are analogous to natural evaporative salt seeding processes commonly experienced by playas (e.g., Rosen 1994).

The misting process represents salt seeding from overland flow or atmospheric wet deposition, a process in which airborne particles accumulated in rain, snow, or fog return to the Earth's surface through precipitation. Salt crystals or crusts form as brackish water sprayed on the soil surface evaporates. Similarly, dissolved salts in brackish water drawn to a soil surface from groundwater sources can recrystallize or form crusts as water evaporates.

The misting approach ensures direct application of salt to the soil surface; however, use of an artificial groundwater source to feed crust formation requires soil matric potential energy (or matric potential) to transfer water from the input source (groundwater) to the soil surface. Put simply, matric potential is the negative pressure potential (i.e., suction) in soil created by the affinity of water molecules to the soil matrix (Hillel 1982). When water enters soil, adsorptive forces (i.e., hydrogen bonding of polar water molecules to oxygen atoms on particle surfaces) attract water molecules to solids in the soil matrix. Soil water molecules are also subject to cohesive forces (i.e., the attraction of water to other water molecules), which are not as strong as the adsorptive forces. This preferential attraction to solid particles over other water molecules creates menisci in water near soil-particle contact points. Tension at the air-water interface induces pressure differentials (i.e., suction) and enables water to move through pore space from zones of higher pressure to lower pressure. This process enables vertical movement of moisture and dissolved salts from groundwater sources to unsaturated soil layers above.

We also explored the sensitivity of crust formation to salinity concentration. Two different brackish water solutions were assessed, one with a concentration of 5000 ppm total dissolved solids (TDS) and one with 10,000 ppm TDS. The TDS of natural playa systems vary and can be well below or in excess of 10,000 ppm (Reynolds et al. 2007). These particular salinity levels, however, were chosen because they represent relatively high and low concentrations found in natural playa systems that we could readily create and maintain in our large-scale setup.

2 Methods

2.1 Meter-scale test-plot design, configuration, and treatment

Six 2 m × 2 m × 1.2 m test plots were constructed out of plywood, 2 in. × 4 in. (5.1 cm × 10.2 cm) lumber, 1 in. (2.54 cm) pine boards, and 4 in. × 4 in. (10.2 cm × 10.2 cm) pressure-treated lumber. Each container was outfitted with a 6 mm thick plastic liner, a drain installed in the corner, and ¾ in. (1.9 cm) PVC perforated pipe grating attached to a stand pipe for water delivery (e.g., Figure 1 and Figure 2). These bases were then covered with about 3 in. (7.6 cm) of pea gravel (approximately 0.4 cm diameter stone) to create the porous substrate necessary for generating an artificial groundwater source.

Each test plot was filled with a loam soil composed of 48% sand, 41% silt, and 11% clay as determined by the hydrometer method (ASTM D7928-17, ASTM International 2017). The organic matter in the soil was 1% as determined by triplicate loss on ignition analyses using a method from Dean (1974). This particular soil mixture is similar in texture to soil samples collected from 38 different playas located throughout the southwestern United States (Natural Resources Conservation Service 2015; Sweeney et al. 2013). Appendix A provides the full dataset, and Table 1 provides additional composition attributes of the fill soil.

Figure 1. Artificial groundwater-delivery assembly in a partially constructed meter-scale test plot.

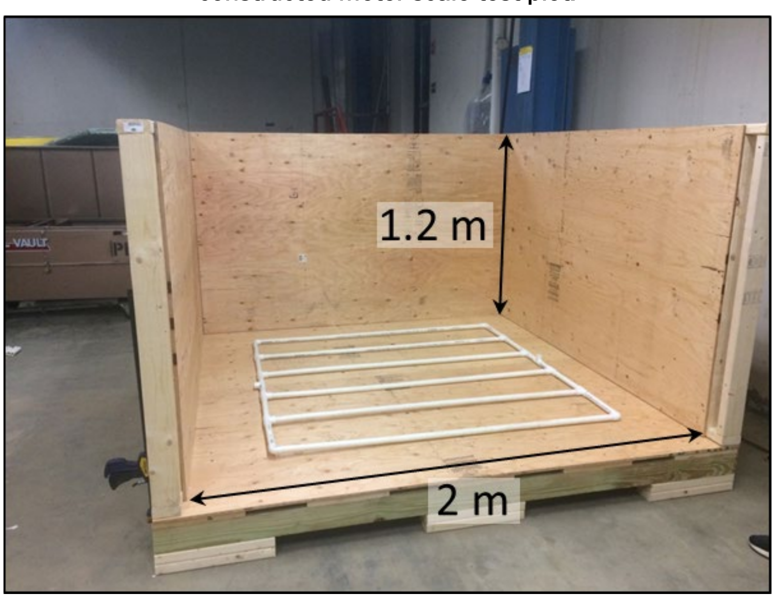

Figure 2. Top-view of a meter-scale test plot with water filling system and stone installed.

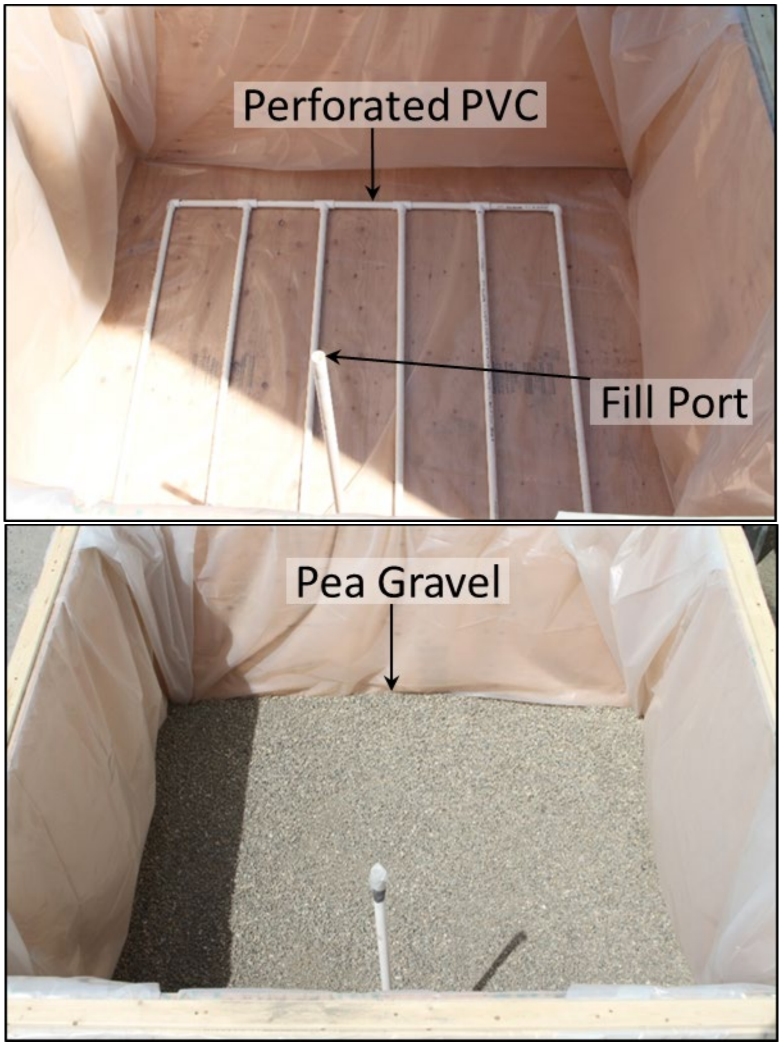

Table 1. Summation of fill soil composition.

Replicate	P (ppm)	K (ppm)	Mg (ppm)	Ca (ppm)	%C	pH 1:1 soil:water	Cation Exchange Capacity ($cmol_c$/kg)
1	3	40	116	2705	0.49	8.2	14.6
2	3	39	115	2697	0.48	7.9	14.5
3	2	38	77	2459	0.46	8.1	13
Avg. ± SD	3 ± 0.6	39 ± 1	103 ± 22	2620 ± 140	0.5 ± 0.02	8 ± 0.2	14 ± 0.9

Prior to packing the plots, the fill soil was spread out, extensively rototilled to break up large aggregates formed during storage, and mixed with water to achieve a 6% gravimetric moisture content. This moisture level was selected to reach a 112 lb ft^{-3} (1794 kg m^{-3}) soil density with the MIL-STD

621A CE-12 modified proctor compaction method (Department of Defense 1964). During the installation process, we increased soil depth by 15 cm at a time (i.e., six vertical inches, known as “six-inch lifts”) and used a Troxler soil density gauge to measure density in five locations after each lift to check for consistency. The center of each plot also contained a Campbell Scientific CS616 moisture probe at a 50 cm depth and two Omega Engineering Inc. Type T (Copper/Constantan) thermocouples at 2 and 50 cm depths, respectively, which were placed in the plots as the boxes were being filled.

The surfaces of the plots were heated with two rows of three 250 W heat lamps. The lamps were positioned 30.5 cm above the soil surface. Each row was 60 cm from either side and had a lamp every 50 cm for equal distribution along the axis of the row (Figure 3).

Figure 3. Top-view of the lighting layout over the meter-scale test plots (*gray* = box frame, *white* = soil, and HL = heat lamp [250 W]).

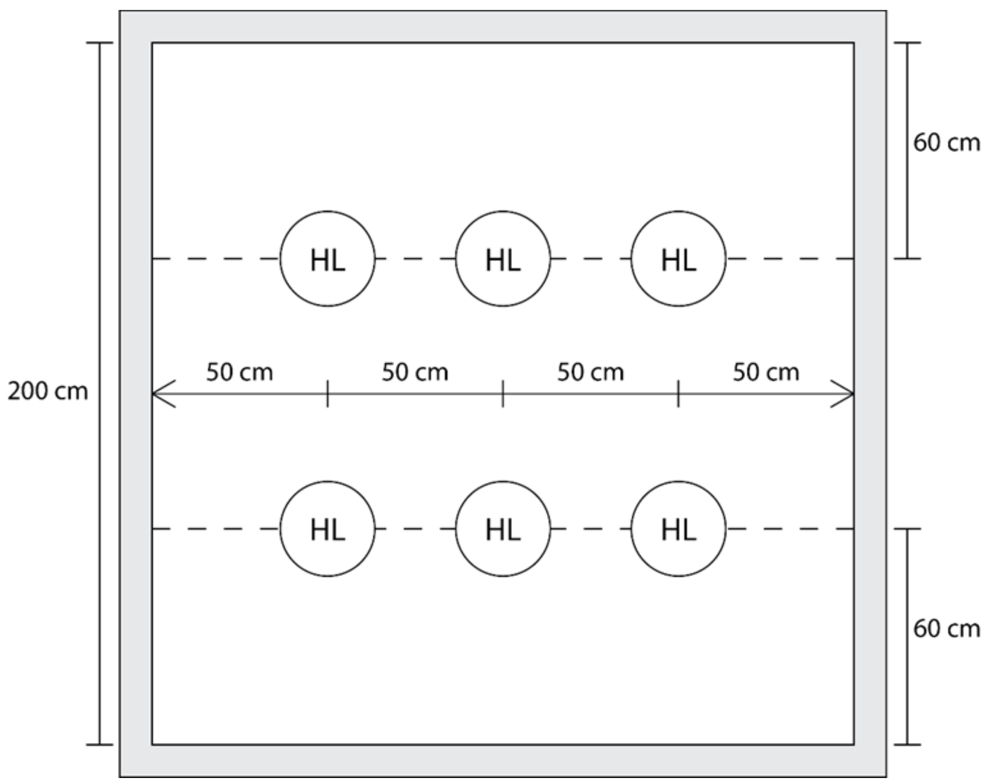

Table 2 and Figure 4 summarize test-plot configurations. Three of the plots were salt seeded using the groundwater method, and the other three were salt seeded using the misting approach. Four of the six plots (two misted and two groundwater) were subject to highly controlled environmental conditions and were covered with two 10 ft × 20 ft (3 m × 6.1 m)

ShelterLogic Greenhouses (referred to as Tent 1 and Tent 2 in Figure 4). Each tent included a 5600 W electric space heater (TPI Corp. model HF686TC) and a DriEaz LGR 2800i dehumidifier set to maintain ambient air temperatures between 95°F to 110°F (35°C and 43°C), surface-soil temperatures near 115°F (46°C), and approximately 15% relative humidity. The remaining two plots (one misted and one groundwater) were left open to the ambient temperature and humidity conditions of the indoor testing facility. Temperature and relative humidity probes were mounted to the side of meter-scale plots 1, 3, and 5 (MS-1, MS-3, and MS-5) at a height of 200 cm above the floor to monitor environmental conditions in Tents 1 and 2 and the ambient conditions of the indoor facility.

Table 2. Experimental meter-scale test-plot configurations.

Plot	Climate	Saltwater-Delivery Method	Salinity TDS Concentration
MS-1	Controlled	Groundwater	5000 ppm
MS-2	Controlled	Misted	5000 ppm
MS-3	Controlled	Groundwater	10,000 ppm
MS-4	Controlled	Misted	10,000 ppm
MS-5	Ambient	Groundwater	10,000 ppm
MS-6	Ambient	Misted	10,000 ppm

Figure 4. Top-view of meter-scale test-plot tenting layout (SM = misted, and GW = groundwater).

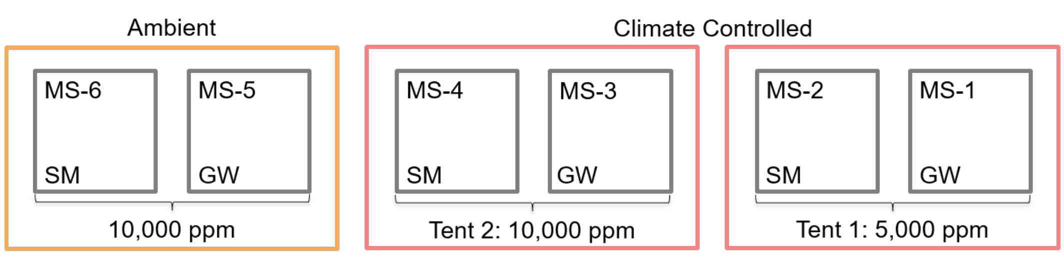

A brackish solution of water (henceforth referred to as saltwater), 5 g/L sodium chloride (NaCl), 2 g/L calcium chloride ($CaCl_2$), 2 g/L magnesium sulfate ($MgSO_4$), and 1 g/L sodium bicarbonate ($NaHCO_3$) was mixed using a mortar mixing drill attachment and added to the plots through gravity feed and misting on a daily basis, Monday through Friday, over the course of 8 weeks. This particular salt mixture was chosen to maximize the likelihood of recrystallization through evaporation and was based on playa surface-soil compositions reported in published literature (e.g., Rosen 1994; Reynolds et al. 2007; Goldstein et al. 2011, 2017). The mixing ratios described above are for dehydrated versions of $CaCl_2$ and $MgSO_4$. These ratios were adjusted to 2.3 g/L and 4.1 g/L for the commercially available hydrated versions, $CaCl_2 \cdot H_2O$ and $MgSO_4 \cdot 7H_2O$, respectively.

Four of the six plots (including the two non-climate-controlled plots, one climate-controlled groundwater plot, and one climate-controlled misted plot) were seeded using a 10,000 ppm saltwater solution, and the other two plots (one climate-controlled groundwater plot and one climate-controlled misted plot) were seeded using a 5000 ppm saltwater solution to investigate the sensitivity of each seeding method to salinity concentration. The TDS levels of each saltwater solution were analyzed prior to application in or on the plots to ensure that salinity concentrations remained relatively consistent throughout the experiment.

After 8 weeks of saltwater treatment, all plots were left undisturbed for a week to allow additional drying. Heat lamps, tents, and climate-control features were then removed so analysts could conduct a series of tests to assess the physical and chemical traits of the plot surfaces.

2.2 Large-scale test-plot design and treatment

We assumed that the misting approach could be used for salt-crust formation on any scale if the technique successfully generated salt crusts on the meter-scale test plots described in section 2.1. However, additional testing was needed to determine the effectiveness of the groundwater-delivery mechanism on surfaces large enough to maneuver vehicles over.

An 18 ft × 24 ft × 3.8 ft (5.5 m × 7.3 m × 1.15 m) test cell was constructed in the Cold Regions Research and Engineering Facility's (CRREL) Frost Effects Research Facility (FERF) (CRREL 2018), outfitted with an artificial groundwater source, and filled with soil. The large-scale test-plot stratigraphy consisted of an XR-5 liner at the base; 15 cm of 1.5 in. (3.8 cm) clean, rounded roofing stone serving as the groundwater source; a layer of nonwoven geotextile; and 1 m of soil installed using the six-inch lift process described in section 2.1.

Two stacks of Campbell Scientific CS616 time-domain-reflectometry soil-moisture probes and collocated Omega Engineering Inc. Type T (Copper/Constantan) thermocouples were installed 100, 75, 50, and 25 cm below the soil surface during plot filling (Figure 5). An additional Type T thermocouple was placed at a 2 cm depth to monitor soil surface temperature over time. These two instrument stacks were located along the center of the long axis at 3.5 m and 7 m from the edge of the plot.

Figure 5. Side view of large-scale test-plot construction and sensor placement (Tr = thermostat, TR = temperature/relative humidity probe, GW = groundwater, T = temperature, MP = moisture probe, and Peak = 3.4 m from the soil surface).

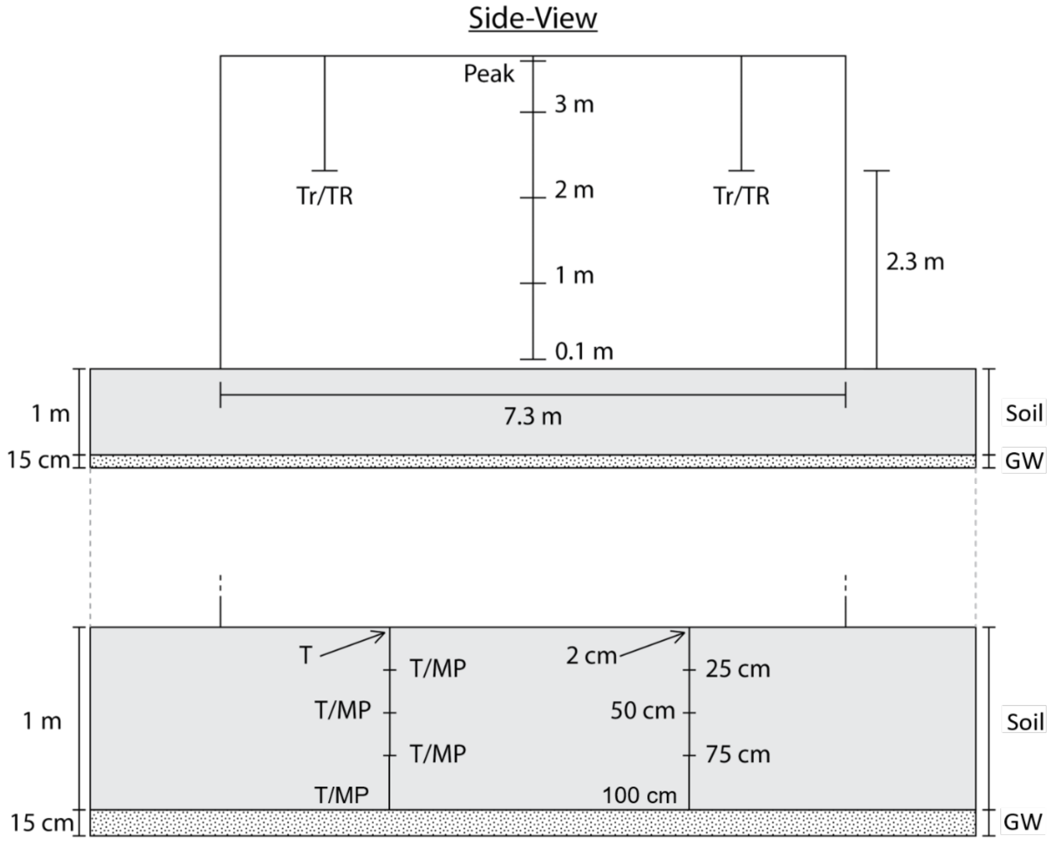

A polycarbonate greenhouse (Figure 6) was assembled and carefully placed on top of the soil surface to allow for temperature and humidity control, and a walkway was constructed through the middle of the greenhouse to allow researchers to access the soil plot and monitor crust formation without affecting the plot surface on either side. Two custom-built parallel lighting tracks were added to the ceiling of the greenhouse to suspend twelve 400 W high-pressure sodium (HPS) lamps 0.75 m above the soil surface (Figure 7). Two additional thermocouples were installed directly under the lighting tracks at a soil depth of 2 cm to monitor soil surface temperatures. Each thermocouple was 1.8 m from either end of the greenhouse and 1.2 m from the greenhouse wall.

Careful measures ensured climate control over the large-scale test plot. Ambient temperature and relative humidity within the greenhouse were monitored via two thermostats suspended 2.3 m above the plot surface, and a thermocouple string was hung from the peak in the center of the greenhouse to monitor air temperatures at various heights (10 cm, 1 m, 2 m, 3 m, and 3.4 m [peak]) above the soil surface (Figure 5 and Figure 7). A ducting system was added to stream heat from an external 15,000 W electric space heater (Fostoria model FES-1524-3E). This heater was connected to the thermocouple 10 cm above the center of the plot surface, which triggered the heater on and off at 43.1°C and 43.3°C, respectively. A DriEaz LGR 2800i dehumidifier was also placed on a platform within the greenhouse to decrease humidity and enhance evaporation from the soil surface.

As with the meter-scale tests, a 5000 ppm TDS saltwater solution (components discussed in section 2.1) was fed to the surface through the groundwater-delivery mechanism for 8 weeks. The large-scale test plot was then allowed to dry for a week, and measurements were taken to assess the physical and chemical traits of the plot surface.

Figure 6. The complete large-scale test plot within CRREL's Frost Effects Research Facility.

Figure 7. Top view of large-scale test-plot greenhouse lighting orientation (T = temperature [vertical thermocouple string], Tr = thermostat, and TR = temperature/relative humidity probe). *Circles* are locations of 400 W HPS lamps, and the *gray shaded* region is the walkway separating the east and west plots.

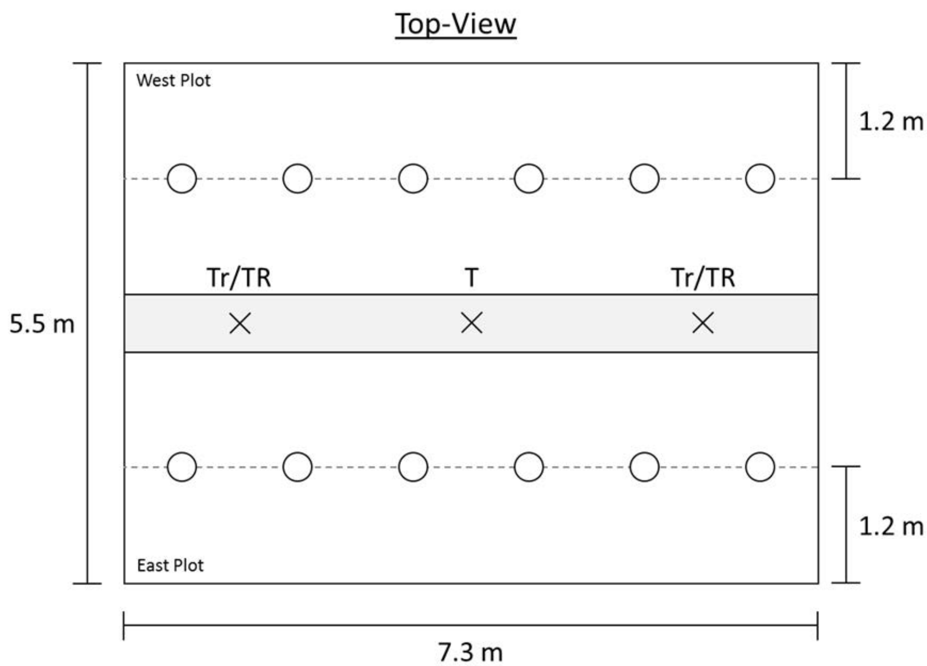

2.3 Crust sampling and analysis

Immediately after heat lamps and environmental controls were removed, analysts collected samples and conducted crust assessment tests on the plots to

1. assess the effectiveness of each technique at forming salt crusts by measuring thickness, shear and compressive strength, and dust-emission potential;
2. quantify crust attribute variability among the various plot configurations; and
3. assess the representativeness of the simulated playa surfaces against published in situ measurements collected from salt-crusted playas in the southwest United States (e.g., King et al. 2011; Reynolds et al. 2007; Goldstein et al. 2011).

For ease of discussion, we refer to the east and west portions of the large-scale test plot (i.e., either side of the walkway, LS-East and LS-West; Figure 7) as two separate "plots" for this crust sampling methodology overview. The two large-scale test-plot portions were each subject to the same sampling and tests conducted on each meter-scale test plot.

Table 3 summarizes our in-plot measurements and their corresponding number of replicates per plot. Analysts collected as many measurement replicates as possible given the complexities of maneuvering equipment without disturbing the crust surface. Sampling locations were selected to maximize surficial coverage and to avoid the outer 15 cm edges of the plot surface, minimizing the sampling crust material influenced by edge effects of the box.

Table 3. In-plot measurements collected for crust assessment.

Attribute Tested	Instrument Required	Number of Replicates
Compressive strength	AMS-59035 pocket penetrometer	7
Shear strength	Humboldt H-4212MH Torvane	7
Dust-emission potential	Portable In-Situ Wind Erosion Lab (PI-SWERL)	3
Crust thickness	Vernier caliper	10

We examined the surface dust-emission potential using a Portable In Situ Wind Erosion Laboratory (PI-SWERL; sampling method and instrument described by Etyemezian et al. 2007). Dust-emission flux measurements for particulate matter of size 10 µm or less (i.e., PM10) were collected on each plot using a peak fan blade rotation of 6000 cycles per minute. Measurements of compressive strength, shear strength, and crust thickness were then collected on the remaining undisturbed portions of the soil surface. Soil crust hardness to the point of rupture was assessed using a pocket geotester or pocket penetrometer with a flat 10 mm diameter foot (AMS #59035, see AMS 2018), crust thickness was measured using Vernier calipers, and shear strength was assessed using a pocket shear vane or torvane (Humboldt H-4212MH).

For further lab-based chemical assessment, three 10 cm × 10 cm (~50 g) crust samples were collected from the remaining intact portions of each plot surface upon completion of the in-plot measurements. Recovered crust samples were dried at 105°C overnight, and percent moisture was calculated by mass loss from drying. Conductivity and pH were measured on 1:5 crust to deionized water slurries and classified as nonsaline, very slightly saline, slightly saline, moderately saline, or strongly saline (e.g., King et al. 2011; Soil Science Division Staff 2017). Aliquots of these slurries were filtered through 0.45 µm filters (Millex IC) and diluted 1000 to 10,000 fold for analysis of soluble ions (Na^+, K^+, Ca^{2+}, Mg^{2+}, Cl^-, NO_3^- , SO_4^{2-}, and PO_4^{3-}) by ion chromatography (Thermo Integrion). We also scraped the surface of crust samples onto adhesive carbon stubs for analysis by scanning electron microscope (SEM) with energy dispersive x-ray spectroscopy (EDS) (Phenom Pro-x) to assess surface bonding and dominant salt crystal shape. The brackish feed water, sampled after each new mix, was measured for anions, cations, and alkalinity (Appendix A). Alkalinity was measured on select water samples by Gran titration using 0.009187 N hydrochloric acid.

During the crust evolution process, we noticed visual differences between plot surfaces that were directly under heat lamps and surfaces outside the immediate heat-lamp exposure (e.g., Figure 8). Samples collected from soils directly under a heat lamp were identified as having a "direct light" treatment and were designated by the label "D" while samples collected outside of the immediate light beam were identified as "indirect light" treatments and were designated by the label "I."

Figure 8. Surficial heterogeneity corresponding to lamp location on meter-scale plots.

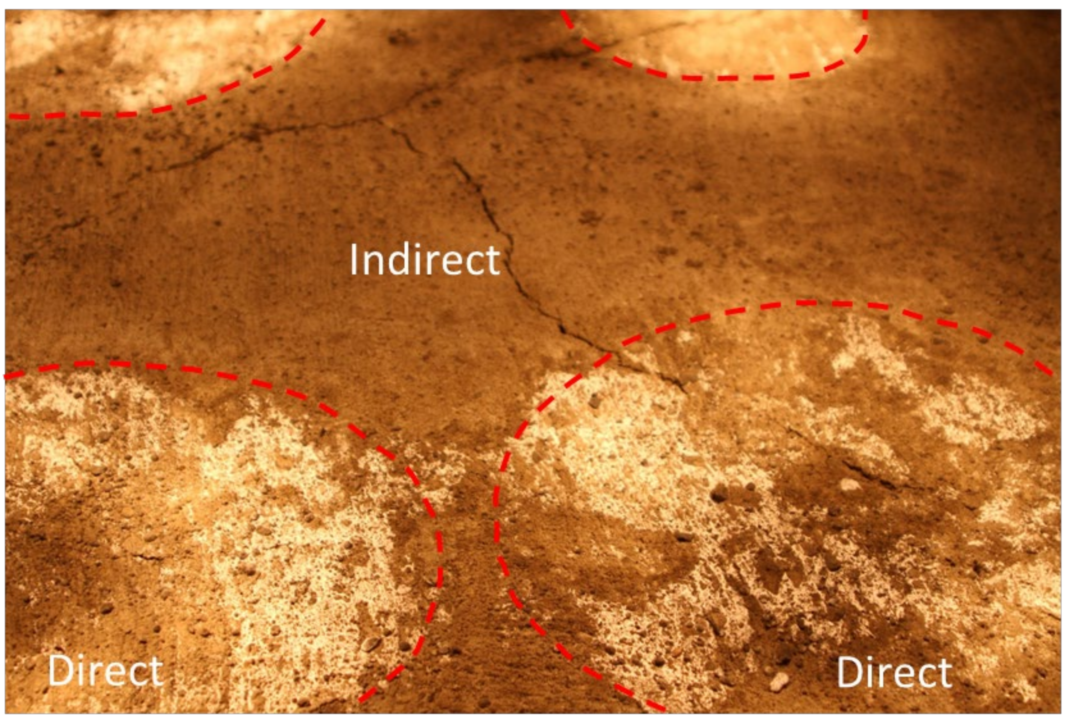

3 Results and Discussion

3.1 Meter-scale test plot—climate control and soil moisture

Table 4 summarizes the average climate conditions for the six meter-scale test plots for the entire testing period. As described in section 2.1, four of the six plots were tented and fed hot air using forced air heaters. These tenting conditions were able to sustain air temperatures of 42.5°C and 40.3°C and relative humidity of 23.0% and 22.1% in Tents 1 and 2, respectively. The ambient climate conditions monitored at MS-5 and MS-6 had average temperature and relative humidity values of 25.7°C and 49.0%, respectively.

Table 4. Average climate conditions for meter-scale test plots.

Enclosure	Plot	Soil Temperature at 50 cm Depth (°C)	Soil Temperature at 2 cm Depth (°C)	Air Temperature (°C)	Relative Humidity (%)
Tent #1	MS-1	37.8 ± 3.2	45.6 ± 2.3[a]	42.5 ± 1.7	23.0 ± 5.2
	MS-2	41.7 ± 4.2	51.6 ± 5.1		
Tent #2	MS-3	39.7 ± 3.6	47.6 ± 3.8	40.3 ± 1.6	22.1 ± 4.5
	MS-4	40.8 ± 4.1	48.3 ± 4.8		
Ambient	MS-5	33.5 ± 2.4	46.0 ± 2.8	25.7 ± 2.7	49.0 ± 7.1
	MS-6	33.7 ± 2.9	41.9 ± 4.2		

[a] MS-1 surface-soil temperature probe became uncovered on 9/7/2017 (day 4) of testing due to surface cracking of soil package.

Surface cracking caused the near-surface thermocouple in MS-1 to shift its position from horizontal placement 2 cm below the soil surface to an upward facing angle about 2 cm above the soil surface (supported by the wire connecting the device to the data logger) on day 4. Thus, the reported 2 cm soil temperatures for MS-1 are erroneous and better reflect near-surface air temperatures from 7 September 2017 through the remainder of the experiment.

Soil moisture was measured in the meter-scale test plots at a depth of 50 cm for the duration of the experiment. Table 5 summarizes the average soil moistures for these plots. The groundwater-fed boxes reached their average soil-moisture values within the first week of the experiment and reached the maximum value within the first 4 weeks (Figure 9).

Table 5. Average soil moisture in meter-scale test plots at a 50 cm depth.

Enclosure	Plot	Soil Moisture at 50 cm Depth (m^3/m^3)
Tent #1	MS-1	0.265 ± 4.8
	MS-2	0.049 ± 4.8
Tent #2	MS-3	0.261 ± 4.8
	MS-4	0.044 ± 4.8
Ambient	MS-5	0.259 ± 4.8
	MS-6	0.055 ± 4.8

Figure 9. Soil moisture through time at a 50 cm depth in the groundwater-fed meter-scale test plots. The break in values is a result of a data-logger error.

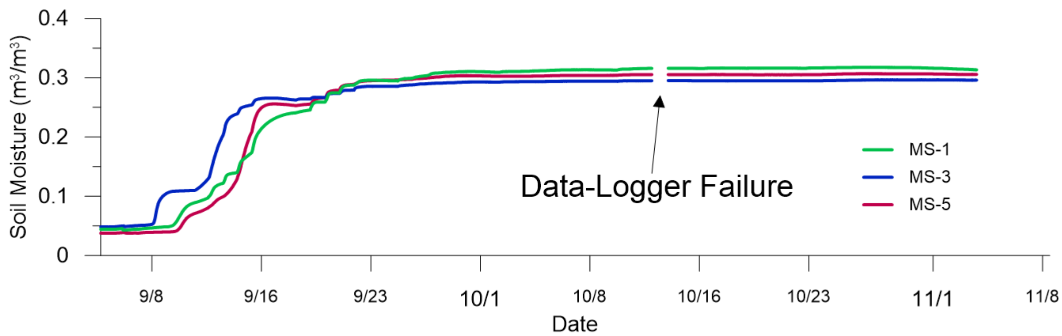

All meter-scale test plots were able to sustain average air and soil temperatures that met or exceeded our target temperature thresholds (Table 4). Even though MS-5 and MS-6 were exposed to ambient temperature fluctuations within the testing space over the 9-week experiment, the surface-soil temperatures were able to maintain an average of 46°C in MS-5 and 41.9°C in MS-6. We attribute this temperature difference to the saltwater-delivery method of each plot. The daily addition of saltwater through misting on MS-6 suppressed the surface temperature. This is apparent when examining the 2 cm soil surface temperature data (Figure 10). When saltwater was added each morning, the soil surface temperature showed a corresponding 10°C drop. This phenomenon was observed in each of the misted plots (MS-2, MS-4, and MS-6). Even though MS-6 did not sustain average temperatures within the desired range, it would rebound to near-target temperatures each day prior to saltwater addition.

Soil surface temperatures were highly sensitive to heat from the overhead lights. A pronounced drop in temperature was recorded in MS-6 on 22–23

September when the overhead lights for MS-6 had to be shut off for approximately 24 hours for building maintenance (Figure 10). It is clear from these data that addition of surface heat is important when attempting to maintain a high surface temperature while misting the plots.

Figure 10. Soil surface temperatures (2 cm) recorded in misted plots over the first 4 weeks of experimentation.

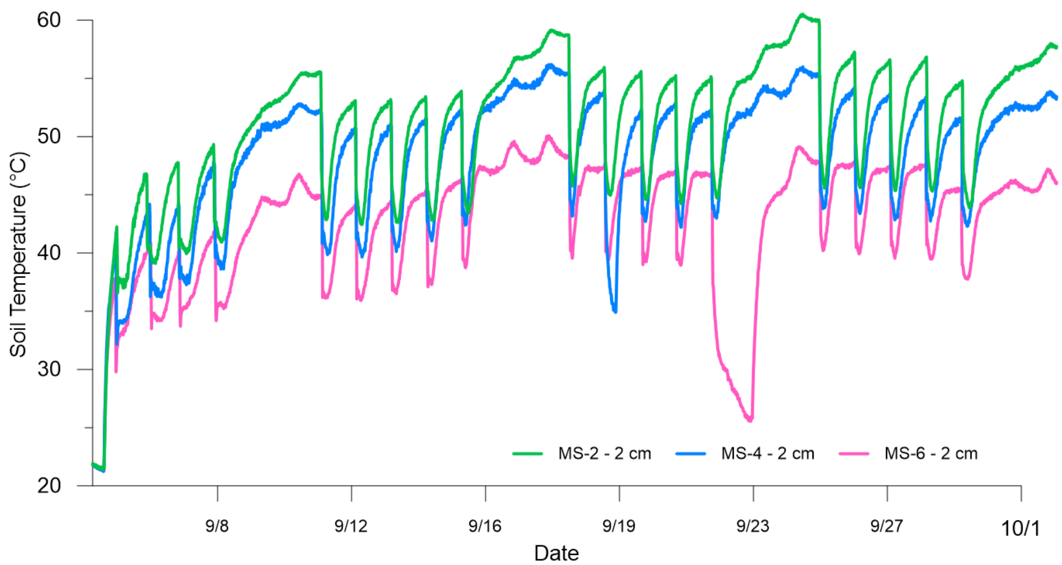

Although Tents 1 and 2 were able to maintain average air temperatures and surface-soil temperatures within our target range, the relative humidity within these spaces (~22% ± 5) did not stay below our target threshold of 15%. We do, however, consider these climate conditions realistic given that relative humidity within southwest United State deserts like the Mojave Desert vary widely and can fluctuate from 10% to 30% during the day to over 50% at night (Desert Studies Center 2015).

Following the addition of saltwater to the meter-scale test plots, we observed several interesting phenomena. First, no matter the heating and dehumidification scheme, the groundwater plots all wicked moisture to the surface over the same general period of time (Figure 11).

The second phenomenon observed was that, after moisture began to reach the surface, soil surface temperatures began to drop and continued to stay in this secondary temperature regime for the remainder of the experiment (Figure 12). On 7 September 2017, the surface-soil temperature probe in MS-1 was uncovered as a result of surface cracking, and therefore the time series in Figure 12 is clipped at that date.

Figure 11. Soil moisture recorded in groundwater plots over the first 3 weeks of experimentation.

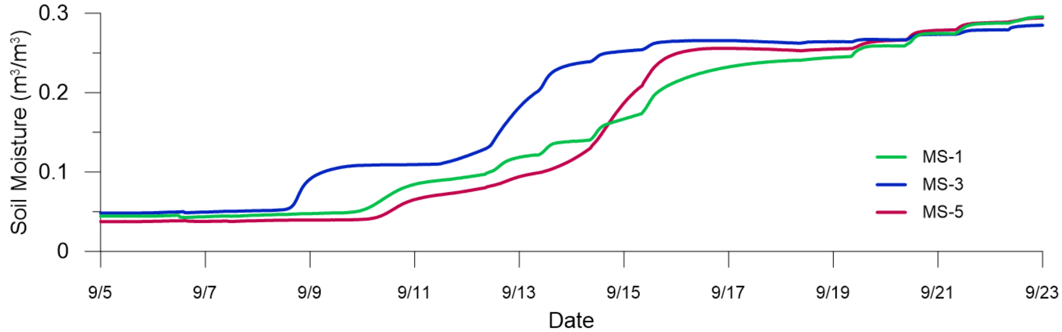

Figure 12. Soil moisture (e.g. “MS-1 - mois”) and surface-soil temperature (e.g. “MS-1 2 cm”) comparison. Note that, as soil moisture increases in the beginning of the experiment, the soil temperature shows a corresponding drop.

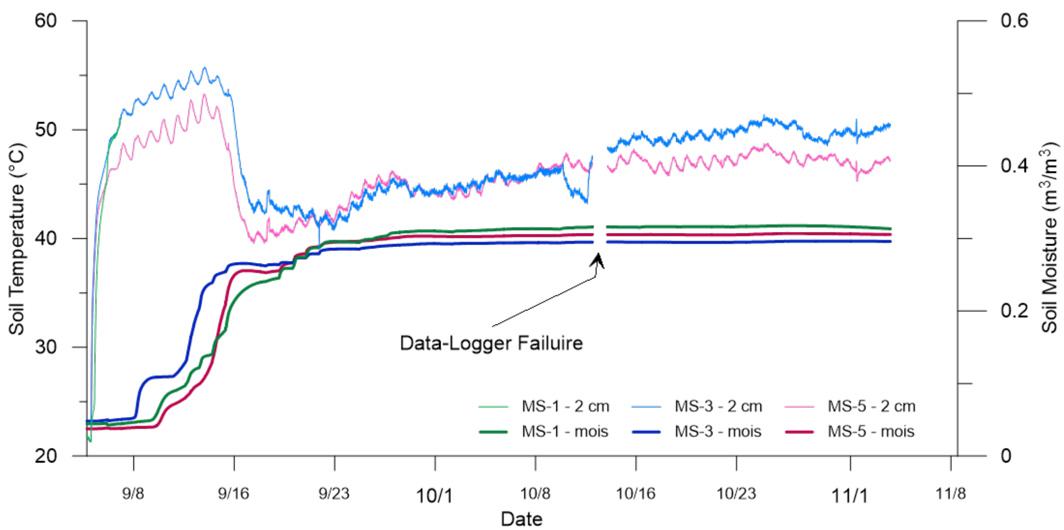

3.2 Large-scale test plot—climate control and soil moisture

Table 6 and Table 7 summarize the average climate conditions for the large-scale test plot during the entire testing period. As described in section 2.2, two sets of temperature measurements were recorded in the large-scale test-plot greenhouse. The first, summarized in Table 6, was a centrally located thermocouple string. The second, summarized in Table 7, was a pair of temperature and percent relative humidity probes mounted 230 cm above the soil surface in the north and south ends of the greenhouse.

Soil temperatures in the large-scale test plot were measured by two stacks of buried thermocouples near the north and south ends of the soil package (Figure 5). Table 8 summarizes the average soil temperatures for these strings. Average soil temperatures decreased with depth in both locations but remained relatively consistent (within 0.1°C) across each depth level (Table 8).

Table 6. Average air temperature values for the central large-scale test-plot thermocouple string.

Height (cm)	Air Temperature (°C)	Standard Deviation (°C)
10	41.3	2.0
100	45.3	1.8
200	46.3	1.8
300	46.5	1.9
340 (peak)	46.0	1.8

Table 7. Average air temperature and percent relative humidity values in the north and south ends of the large-scale test-plot greenhouse (exact locations shown in Figs. 5 and 7).

Location	Air Temperature (°C)	Relative Humidity (%)
North End	46.9 ± 1.8	9.7 ± 2.2
South End	48.0 ± 1.7	15.4 ± 4.8

Table 8. Average soil temperature values in the north and south ends of the large-scale test-plot soil package (exact locations in Figs. 5 and 7).

Depth (cm)	Soil Temperature South (°C)	Standard Deviation South (°C)	Soil Temperature North (°C)	Standard Deviation North (°C)
2	36.0	3.2	36.2	4.2
25	32.4	1.7	32.3	1.9
50	30.3	2.1	30.3	1.8
75	28.4	2.4	28.4	1.9
100	27.0	2.4	27.1	2.2

Soil moisture was measured in the large-scale test plot at depths of 25, 50, 75, and 100 cm in the north and south ends of the soil package (Figure 5). Table 9 summarizes the average soil moisture in these locations.

The south end of the large-scale test plot reached near maximum soil-moisture values measured within the first 3 weeks of testing (Figure 13). The north end of the large-scale test plot reached near maximum soil-moisture values measured in just over 5 weeks of testing; however, the moisture content of the soil as recorded by the 25 cm probe was still increasing on the final day of the study (Figure 14).

Table 9. Average soil moisture in the large-scale test plot at the north and south end of the soil package.

Depth (cm)	Soil Moisture South (m^3/m^3)	Soil Moisture North (m^3/m^3)
25	0.23 ± 0.06	0.130 ± 0.07
50	0.27 ± 0.05	0.199 ± 0.1
75	0.33 ± 0.04	0.233 ± 0.1
100	0.34 ± 0.02	0.270 ± 0.08

Figure 13. Soil moisture through time in the south end of the large-scale test plot.

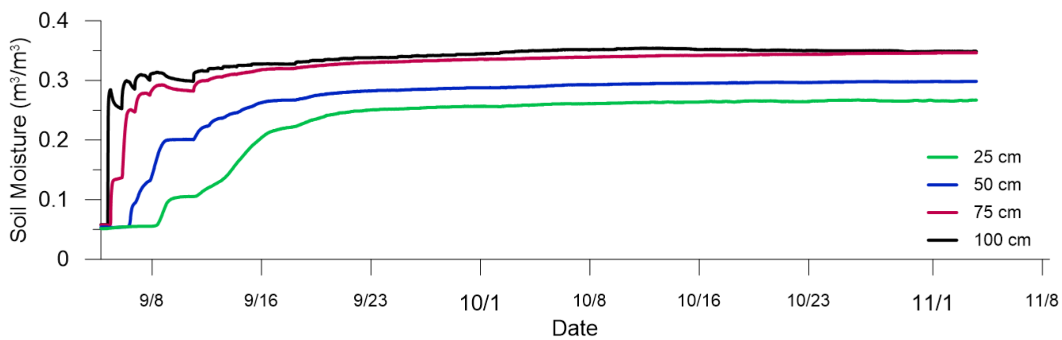

Figure 14. Soil moisture through time in the north end of the large-scale test plot.

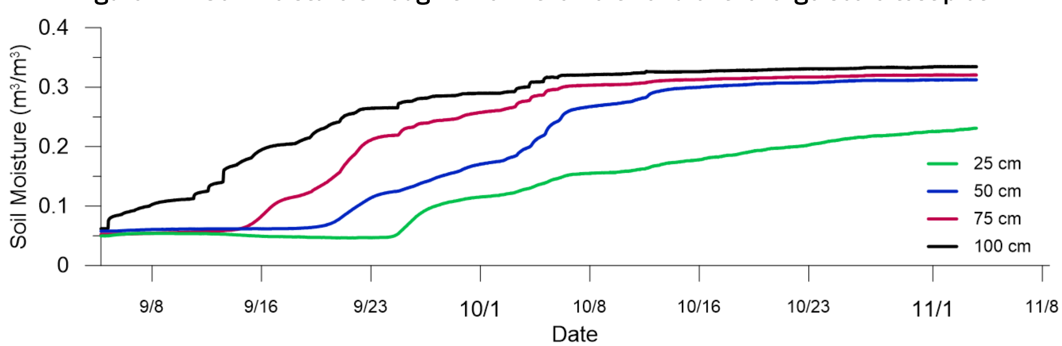

This pattern of moisture, first showing in the southeastern corner and spreading laterally until it reached the entire surface, was most likely due to our groundwater source design. Saltwater solution was fed in through the southeastern corner of the plot at the deepest part of the artificial groundwater source. This affected how the moisture was eventually delivered to the surface as shown in Figures 13 and 14.

The large-scale test plot was able to maintain or exceed target values for air temperatures and relative humidity (Table 6 and Table 7). When examining the long-term trend of air temperature within the greenhouse, we observed three distinct phases. Phase 1 was a relatively stable period from the start of the experiment to 11 September 2017 (day 8) when the lighting protocol was changed to daytime-only operation. When we were operating the heat lamps 24 hours/day, the internal components of the lights overheated and started to fail. After replacing three lights over the course of the first week, we changed our procedure from keeping the lights on all of the time to keeping the lights on only during work hours (0700–1530 ET, Monday–Friday). Following this experimental design change, a stronger diurnal temperature swing was observed in the data, which represents Phase 2 (Figure 15). Average temperatures remained relatively high (42.75°C ± 0.07) over Phase 2.

Figure 15. Air temperature of the large-scale test plot compared to ambient temperature within the FERF. Air temperatures are 11-point moving averages, and the ambient (*tan*) is a 91-point moving average. Note the three separate temperature regimes shown by the *yellow*, *green*, and *orange bars*.

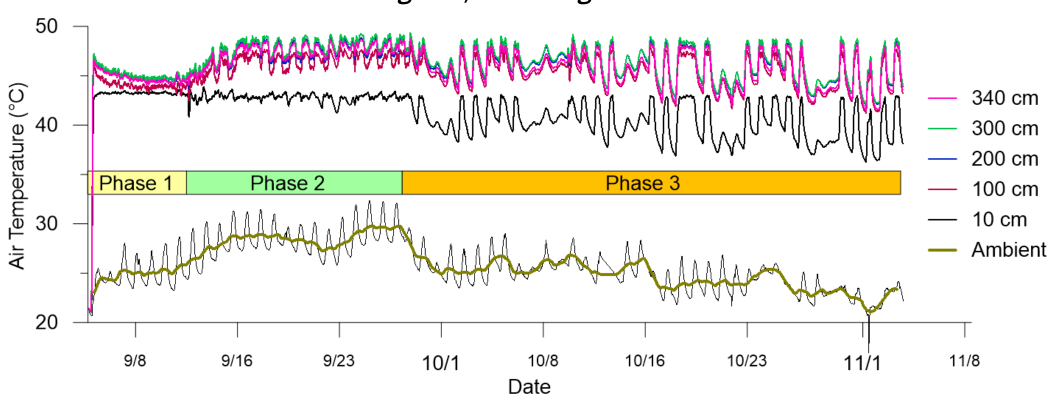

A third temperature phase (Phase 3) with much more pronounced diurnal variation began around 27 September 2017 (day 24). Over the course of Phase 3, the overall average temperature dropped and became more variable (41.00°C ± 1.86). As shown in Figure 15, these temperature patterns corresponded to a similar drop in ambient temperatures surrounding the test area. Even so, the average air temperature remained within our target range throughout the duration of the entire experiment despite the failure of our climate-control system to fully neutralize temperature fluctuations of the surrounding environment. Trends in the large-scale test-plot surface-soil temperature reflected both the timing of saltwater delivery to the plot surface and the air temperature (Figure 16). This same phenomenon was also observed in the meter-scale boxes.

Figure 16. Comparison graphs of soil temperature at 2 and 25 cm depths and soil moisture at a 25 cm depth. Data for the north is the *top* time series, and data for the south is the *bottom* time series.

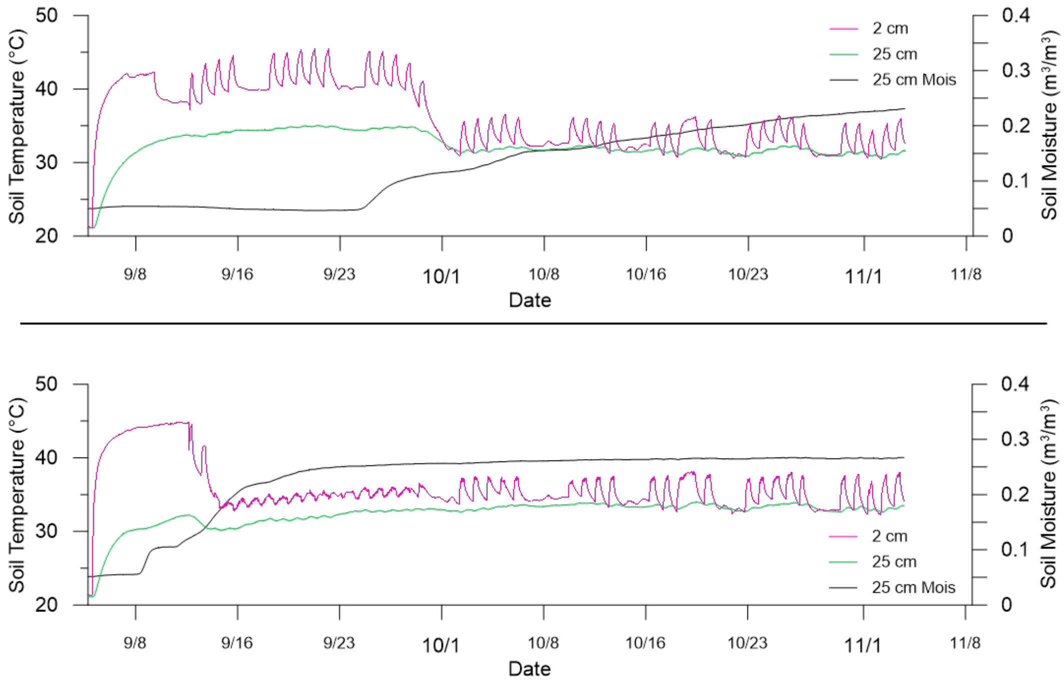

3.3 Large- and meter-scale test-plot chemistry

Table 10 summarizes the average crust chemistry data for meter-scale plots 1–6; Appendix B presents the full dataset. The average pH of surface-crust samples ranged from 7.8 to 9.7 with most classified as moderately alkaline to strongly alkaline and MS-6 being very strongly alkaline. The average electrical conductivity ($EC_{1:5}$) of the surface-crust slurries varied from near 0 in MS-2 to 74.2 mS/cm in MS-5. The wide range of $EC_{1:5}$ relative standard deviations (RSDs) shown in Table 10 indicate compositional heterogeneity within crusts at the 10 cm scale. The salinity class of these soils, as indicated by $EC_{1:5}$, were mostly moderately or strongly saline; and these classifications were supported by total cation and anion concentrations (e.g., King et al. 2011; Soil Science Division Staff 2017).

Table 10 summarizes the average crust chemistry data for the east (LS-E) and west (LS-W) plots of the large-scale test plot (full dataset in Appendix B). The average pH of crust samples ranged from 8.2 to 8.3 with RSDs near 1%. All samples were classified as moderately alkaline and slightly to moderately saline based on $EC_{1:5}$ measurements (King et al. 2011; Soil Science Division Staff 2017). The average $EC_{1:5}$ of the surface-crust slurries varied from 7.3 to 12.6 mS/cm. RSD values summarized in Table 10 ranged from 19% to 53%. It is important to note that the dissolved ions within the groundwater-fed crusts are roughly an order of magnitude higher than those measured in the misted crusts (discussed in detail at the end of this section).

Table 10. Summary of crust chemistry measurements for large- and meter-scale test plots. Data points are averages of triplicate crust samples.

	1:5 Extraction			Dissolved Ions from 1:5 Extraction (mg/kg)							
Sample ID	pH	$EC_{1:5}$ (mS/cm)	$EC_{1:5}$ (RSD %)	Na^+	K^+	Mg^{2+}	Ca^{2+}	Cl^-	SO_4^{2-}	NO_3^-	PO_4^{3-}
MS-1-I-Avg	7.9	40.7	14	2E+04	3E+01	1E+03	2E+04	7E+04	2E+04	2E+03	<600
MS-1-D-Avg	7.8	47.5	5	2E+04	6E+01	1E+03	2E+04	8E+04	6E+03	4E+03	<600
MS-2-I-Avg	8.7	1.1	24	4E+02	3E+00	4E+01	3E+02	7E+02	1E+03	<60	<60
MS-2-D-Avg	8.9	0.8	31	3E+02	3E+00	4E+01	2E+02	7E+02	7E+02	<60	<60
MS-3-I-Avg	8.0	64.7	16	5E+04	4E+01	1E+03	2E+04	1E+05	1E+04	2E+03	<600
MS-3-D-Avg	8.0	72.2	10	5E+04	1E+02	2E+03	3E+04	1E+05	4E+03	1E+03	<600
MS-4-I-Avg	8.8	5.9	22	3E+03	1E+01	3E+02	3E+03	6E+03	9E+03	<60	<60
MS-4-D-Avg	9.6	8.7	39	6E+03	4E+01	5E+02	1E+03	1E+04	4E+03	<60	<60
MS-5-I-Avg	8.1	38.9	77	2E+04	4E+01	1E+03	2E+04	7E+04	1E+04	2E+03	<600
MS-5-D-Avg	7.9	74.2	19	5E+04	8E+01	3E+03	3E+04	1E+05	5E+03	2E+03	<600
MS-6-I-Avg	9.0	10.3	8	6E+03	3E+01	7E+02	3E+03	1E+04	1E+04	<60	<60
MS-6-D-Avg	9.7	23.2	14	2E+04	1E+02	1E+03	3E+03	4E+04	6E+03	<60	<60
LS-E-I-Avg	8.2	8.2	35	8E+02	2E+01	4E+02	8E+03	8E+03	1E+04	1E+03	<60
LS-E-D-Avg	8.2	12.6	53	2E+03	3E+01	8E+02	1E+04	2E+04	1E+04	2E+03	<60
LS-W-I-Avg	8.3	7.3	21	8E+02	1E+01	3E+02	7E+03	7E+03	1E+04	2E+03	<60
LS-W-D-Avg	8.2	11.4	19	1E+03	2E+01	7E+02	1E+04	1E+04	1E+04	2E+03	<60

The crust chemistry data were further analyzed to assess correlations between the measured variables. A Box-Cox transformation was applied to the measured variables to more closely approximate normal distributions for downstream parametric statistical analyses (e.g., Box and Cox 1964) (Figure 17).

The chemistry data were first analyzed using a hierarchical cluster analysis following Ward's Method to assess relationships among the derived chemical profiles (Ward 1963) (Figure 18). Results, depicted in a two-way dendrogram (Figure 18), highlight a distinct difference between the water chemistry data obtained from plots that were misted and from plots that were fed by groundwater. Meter-scale test plots, misted versus groundwater fed, and large-scale test plots clustered separately.

Figure 17. Results of Box-Cox transformation when applied to the K^+ data. Originally distributed data is on the *left*, and transformed data is on the *right*.

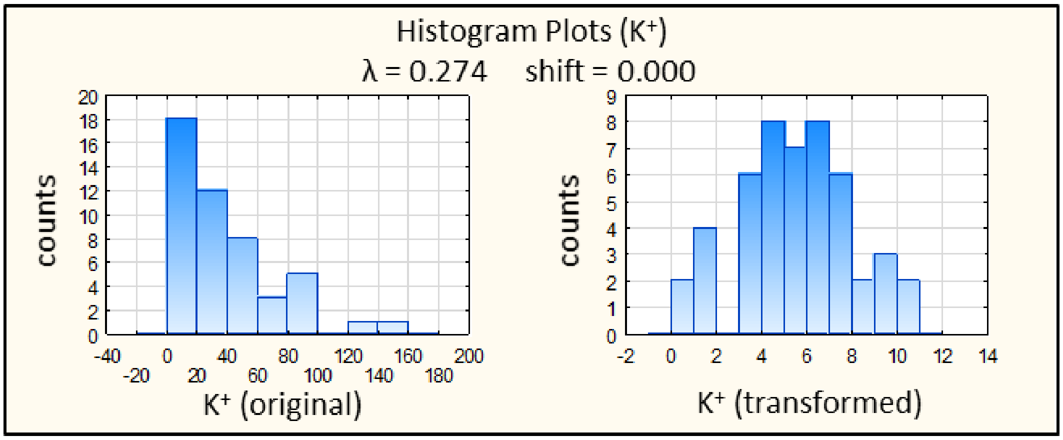

Figure 18. Results of hierarchical cluster analysis of transformed chemistry data.

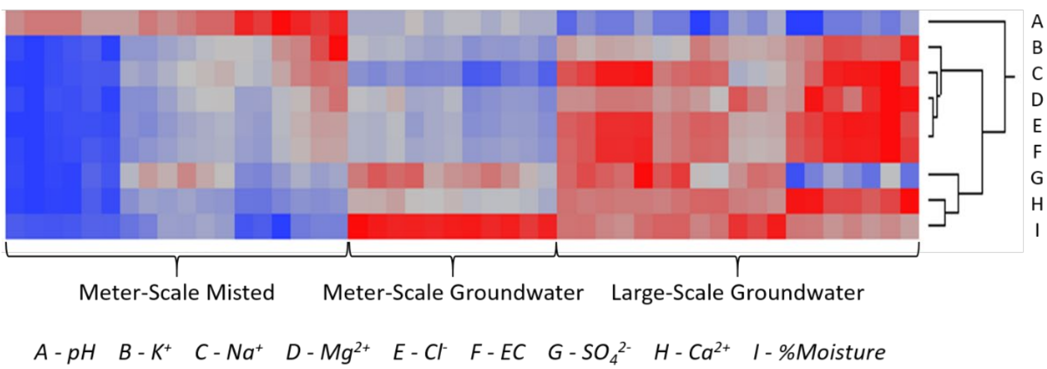

A principal component analysis (PCA) was then performed to further explore which variables were most strongly associated with the observed differences between the misted- and groundwater-fed crusts (Figure 19).

Figure 19 depicts the results from the PCA. The two-dimensional plot illustrates the first two principal components with the scores (samples) indicated by the symbols and the loadings (variables) indicated by the line vectors. The misted- (green circles) and groundwater- (hollow red circles) fed crust samples clustered separately, which was in agreement with the hierarchical cluster analysis. The large-scale test-plot samples (triangles) also associated in a separate cluster. Within the meter-scale-plot misted sample grouping (green oval), we observed a cluster of the crust samples that were treated with 5000 ppm TDS saltwater (black oval).

Sample pH was the most heavily weighted variable in describing the meter-scale-plot misted (green circle) samples. This result could be due to a preferential concentration of carbonate on the surface of the misted plots (e.g., Table 10) due to the direct delivery of the saltwater mix. Carbonate within the groundwater-fed systems may have precipitated out prior to reaching the surface, which led to crust compositions that were less alkaline than observed in the misted crusts. This phenomenon may also be responsible for the identification of greater ionic species concentration, and moisture, in the groundwater-fed meter-scale plots.

Figure 19. Results of the principal component analysis of crust chemistry data (MS = meter-scale, LS = large-scale, GW = groundwater, and SM = misted).

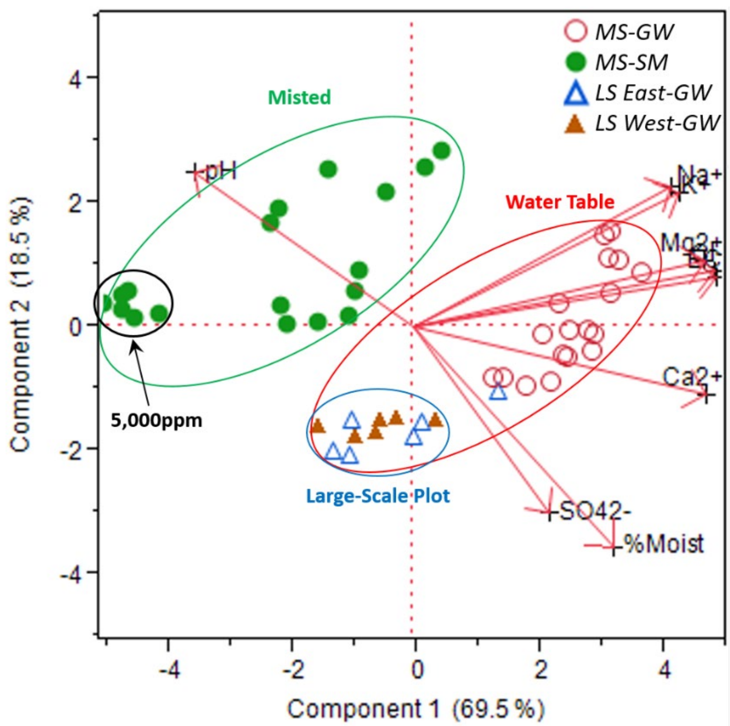

Variable means were then compared via a one-way analysis of variance (ANOVA) using a post-hoc Tukey honest significant difference (HSD) measure (Tukey 1949). These analyses were performed to determine the statistical significance of the saltwater-delivery mechanism, the sampling location with respect to the heat lamps, and the level of climate control on crust chemistry. Figures 20–22 show the results for sample pH and $EC_{1:5}$ (all results in Appendix C). The points within these plots are individual sample values, the box plot itself shows a center line that represents the sample's median value, and the ends of the box are the 75th and 25th quantiles. The large whiskers represent the 1st and 3rd quartile and the small whiskers the standard deviation about the mean. Significance was determined at an alpha level of 0.05.

Figure 20. Results of the one-way ANOVA test of transformed pH and $EC_{1:5}$ data based solely on saltwater-delivery method (GW = groundwater, and SM = misted).

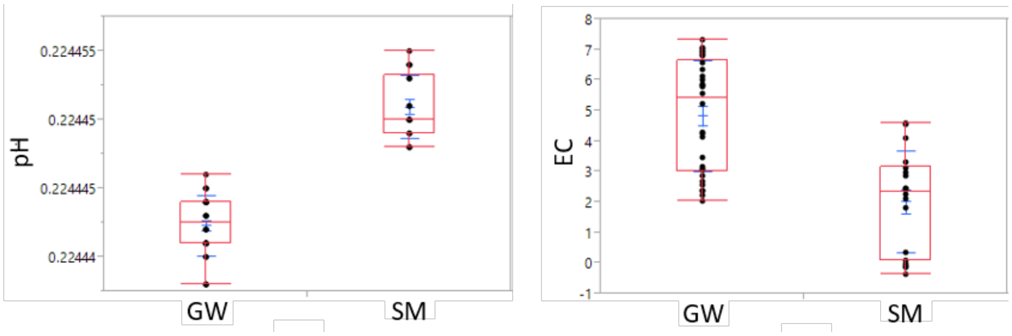

Figure 21. Results of the one-way ANOVA test of transformed pH and $EC_{1:5}$ data based on saltwater-delivery method, sampling location, and TDS of feed saltwater (GW = groundwater, and SM = misted). (Ambient boxes excluded.)

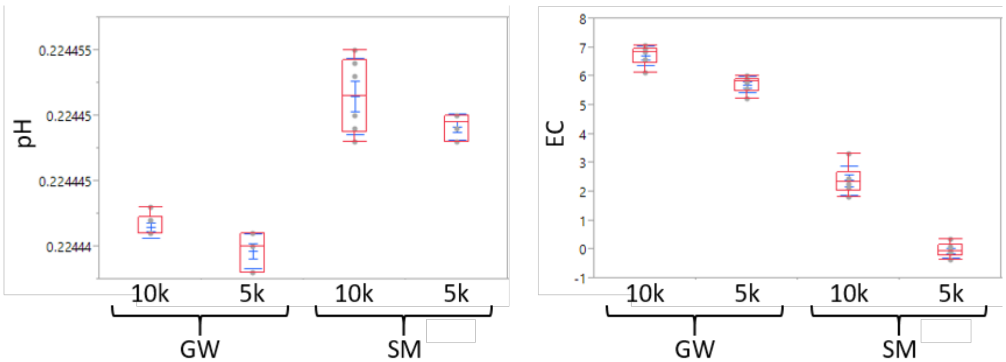

Figure 22. Results of the one-way ANOVA test of transformed pH and $EC_{1:5}$ data based on the saltwater-delivery method, the sampling location, and heated tents versus ambient (GW = groundwater, SM = misted, D = direct lighting, and I = indirect lighting).

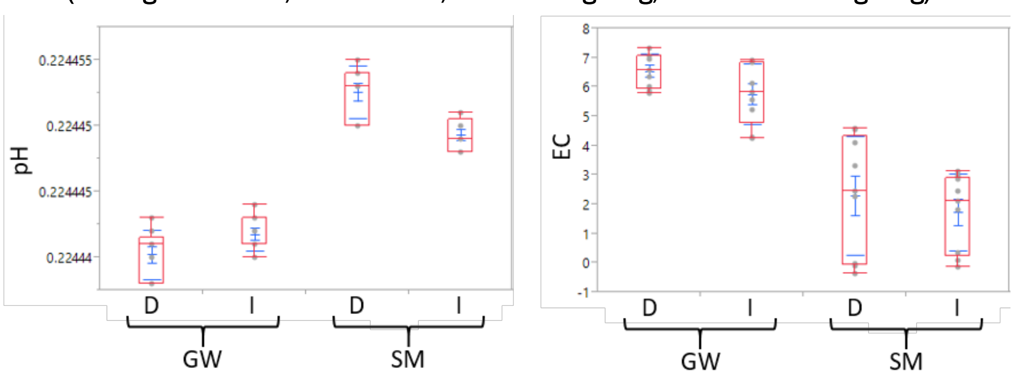

Results identified a statistically significant difference between the two saltwater-delivery methods on crust composition. This observation held true for all measured variables (see Appendix C). There was also a significant secondary effect from the lighting system that was most pronounced in pH, moisture content, SO_4^{2-}, and Ca^{2+} ion presence (large-scale test-plot samples excluded). This was most likely due to increased heat exposure in samples collected directly under the lights, leading to increased evaporation. The TDS of the saltwater also resulted in a significant effect on crust composition in samples collected from the tented plots. The TDS influence was most pronounced in surface-crust ion levels and appeared to affect the misted plots more than those fed by groundwater. This result was somewhat intuitive since the direct application of saltwater in the misted approach would result in a greater relative change in crust chemistry composition when comparing the 5000 ppm and 10,000 ppm misted crusts. Groundwater-fed crusts form by evaporation of saltwater filtered by the soil matrix, which could have a buffering effect on the total evaporate (ion) content in the resulting crust, as described by the matric potential. In short, findings indicate that the saltwater-delivery method clearly affected the chemical composition of the resulting crusts. As mentioned previously, the groundwater-fed crusts, although less different than one another, have a much higher dissolved ion content than the misted crusts. We postulate that this is most likely due to the greater amount of saltwater added to keep the groundwater source full rather than an enhancement of evaporative processes at the surface of the groundwater-fed plots.

3.4 Large- and meter-scale test-plot physical crusting

Table 11 summarizes the physical characteristics of the meter-scale test-plot crusts. Average crust thickness varied from 2.14 to 4.65 mm with RSDs from 17% to 43%. Compressive strength measurements varied from a low of 0.04 kg cm^{-2} to a high of 0.87 kg cm^{-2}. Average shear strength values ranged from 0.033 to 0.295 kg cm^{-2} with a wide range of RSDs from 16% to 76%.

When analyzing crust samples for crystal shape and composition by SEM-EDS, we observed a variety of crystal shapes and compositions (Figure 23). Columnar crystals of NaCl were present in both misted- and groundwater-fed boxes. Many surfaces of grains in the misted boxes also had coatings composed of (1) Ca, O, and S and (2) Na, O, and Cl. We also observed discontinuous crystal growth in the misted plots, which resulted in crystal habits full of voids, giving them a “holey” or “Swiss cheese” appearance. Although not shown in Figure 23, platy crystal habits were also produced by both saltwater-delivery methods and were most commonly composed of either Ca, Si, and O or Ca, S, and O with some occurrences of Ca, O, Cl and Ca, O, Cl, and Mg (measured by EDS) (Appendix B). Determining the exact mineralogical makeup of these crystals was beyond the scope of this study; but we collected, homogenized, and archived three additional 10 cm × 10 cm (~50 g) crust samples from each plot should additional testing be warranted. By examining mineralogy, there is the potential to compare simulated crusts to individual real-world locations.

Table 11. Summary of physical crust measurements from meter-scale test plots. Data points are averages of triplicate crust samples. Compressive and shear strengths were measured at least seven times, and crust thickness was measured ten times for each average shown below.

Tenting	Plot #	Lighting	Water Feed	Thickness (mm)	Thickness RSD (%)	Compressive Strength (kg/cm²)	Compressive Strength RSD (%)	Shear Strength (kg/cm²)	Shear Strength RSD (%)
Tent #1	MS-1	Direct	Groundwater	3.63	28	0.27	34	0.156	63
	MS-1	Indirect	Groundwater	3.67	27	0.70	61	0.033	43
	MS-2	Direct	Misted	2.87	34	0.75	22	0.133	50
	MS-2	Indirect	Misted	3.15	33	0.70	61	0.028	28
Tent #2	MS-3	Direct	Groundwater	4.65	27	0.36	29	0.295	16
	MS-3	Indirect	Groundwater	2.85	34	0.35	49	0.074	76
	MS-4	Direct	Misted	2.14	26	0.04	30	0.067	60
	MS-4	Indirect	Misted	2.70	22	0.37	40	0.041	24
Ambient	MS-5	Direct	Groundwater	3.48	43	0.25	67	0.148	51
	MS-5	Indirect	Groundwater	2.47	17	0.26	31	0.039	38
	MS-6	Direct	Misted	3.94	20	0.87	20	0.064	53
	MS-6	Indirect	Misted	2.60	25	0.21	94	0.033	63

Figure 23. Scanning electron microscope images of selected crystal shapes and crust bonding. Plot number are indicated in the *upper left* corners of the images. *MS-1*: columnar NaCl crystals; *MS-3*: Ca, Cl, O, C crystal with void structure; *MS-6* (*left*): stacked columnar NaCl crystals; *MS-6* (*right*): surface coating of large grains.

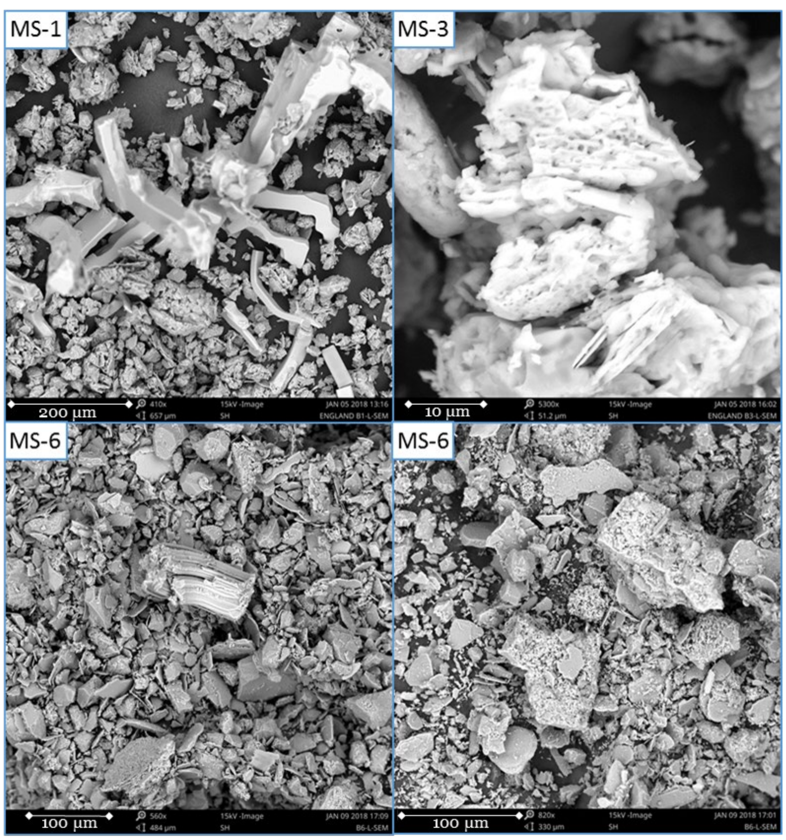

Figures 24 and 25 summarize dust-emission potential measurements for the meter-scale test plots. PI-SWERL ramp tests were used to establish average dust-emission fluxes using fan blade speeds of approximately 4000, 5000, and 6000 revolutions per minute (rpm). These blade speeds roughly equate to 10 m wind speeds of 12.4, 15.2, and 18.1 m s^{-1} (approximately 28, 34, and 40 mph), respectively. Figure 24 shows that dust-emission fluxes were generally low (expected for crusted soils); and in most cases, the average flux for triplicate measurements increased with fan speed. Meter-scale plots MS-2 (direct lighting) and MS-4 (indirect lighting) were an exception. These plots experienced a decrease from 4000 to 5000 rpm for their measurements. Furthermore, meter-scale plots MS-2, MS-4, and MS-6 produced dust-emission fluxes that were an order of magnitude larger than the rest of the plots at 6000 rpm, and in the case of MS-2, at 5000 rpm as well. These three plots were fed saltwater though misting but had different lighting and climate-control conditions.

Table 12 summarizes physical crust characteristics exhibited by the large-scale test plot. Average crust thickness varied from 2.8 to 4.18 mm with RSDs from 20% to 29%. Compressive strength measurements varied from a low of 0.18 kg cm^{-2} to a high of 0.24 kg cm^{-2}. Average shear strength values ranged from 0.046 to 0.054 kg cm^{-2} with a range of RSDs from 11% to 16%. Most of these values are similar to those measured for the meter-scale plots fed by groundwater, except for shear strength, which tended to be lower.

Figure 24. Average dust-emission fluxes (mg m^{-2} s^{-1}) for all meter-scale test plots measured by PI-SWERL.

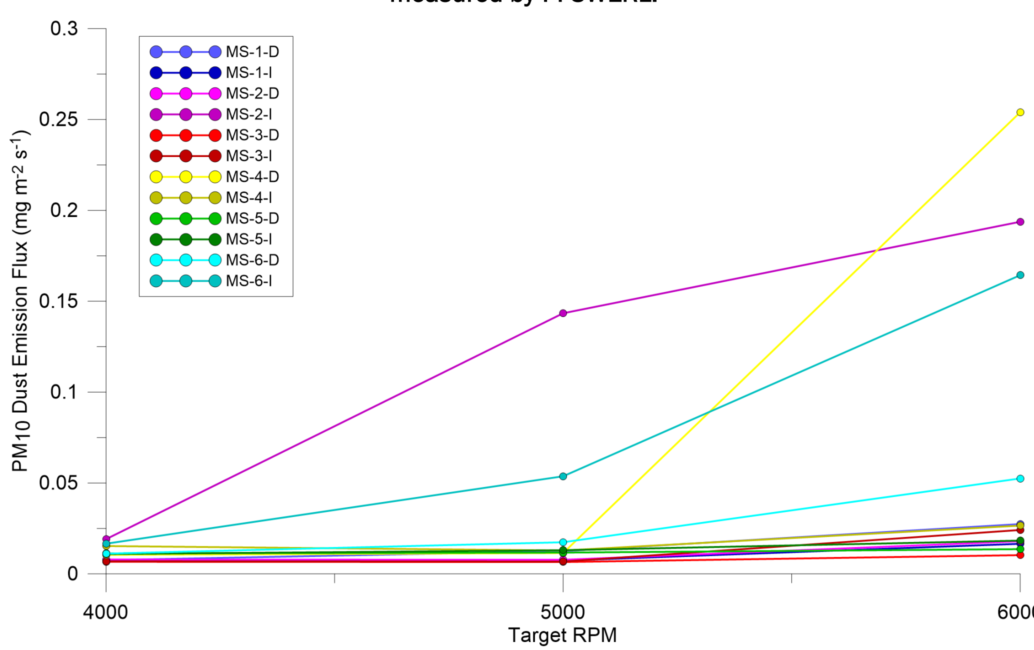

Figure 25. Average dust-emission fluxes <0.03 mg m⁻² s⁻¹ for meter-scale test plots 1–5 (excluding MS-4-D).

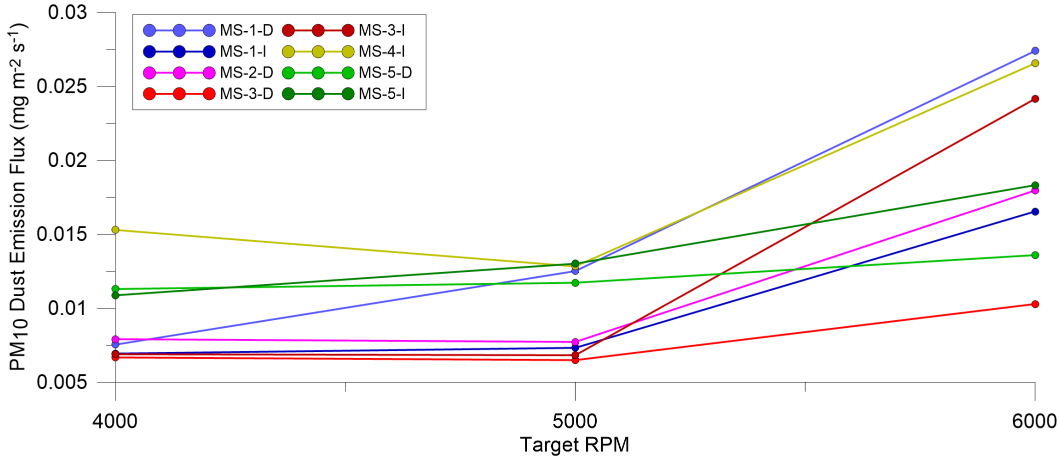

Table 12. Summary of physical crust measurements from the large-scale greenhouse test plot. Data points are averages of triplicate crust samples, keeping with sampling described for the meter-scale test plots. (LS = large-scale).

Plot	Lighting	Water Feed	Thickness (mm)	Thickness RSD (%)	Compressive Strength (kg/cm2)	Compressive Strength RSD (%)	Shear Strength (kg/cm2)	Shear Strength RSD (%)
LS-West	Direct	Groundwater	2.80	29	0.20	24	0.046	12
LS-West	Indirect	Groundwater	3.96	20	0.18	17	0.054	11
LS-East	Direct	Groundwater	4.18	21	0.24	25	0.054	16
LS-East	Indirect	Groundwater	4.11	28	0.21	22	0.050	15

When analyzing the large-scale test-plot crust samples for crystal shape via the SEM, the dominant crystal shapes we observed were platy (Figure 26). Upon further analysis of the east and west sections, we determined these platy crystals were calcium sulfate ($CaSO_4$) and that the crystals from the east side of the plot exhibited linear surface fractures. $CaSO_4$ crystals also occurred in clusters of plates. These results are consistent with what we observed in the meter-scale plots; platy clusters of this composition appeared in both cases.

Figure 27 summarizes large-scale test-plot dust-emission-potential results. We used the same ramp test (4000, 5000, and 6000 rpm) on the east and west sections of the large-scale test plot that we used to assess the meter-scale test plots. Figure 27 shows that, in all cases, the average flux for triplicate measurements increased with rpm. However, this pattern did not always hold true when results were separated by lighting position. The west plot produced slightly higher dust-emission fluxes than the east plot, though these values only differed by about 0.002 mg m^{-2} s^{-1}. The dust-emission flux measurements for the large-scale plot tended to be an order of magnitude lower than measurements from the meter-scale plots measured at the same rpm.

Figure 26. SEM images of platy crystals sampled from the large-scale test plot. *LS-E*: platy $CaSO_4$ crystals with linear fractures; *LS-W*: $CaSO_4$ crystals in plates and platy clusters.

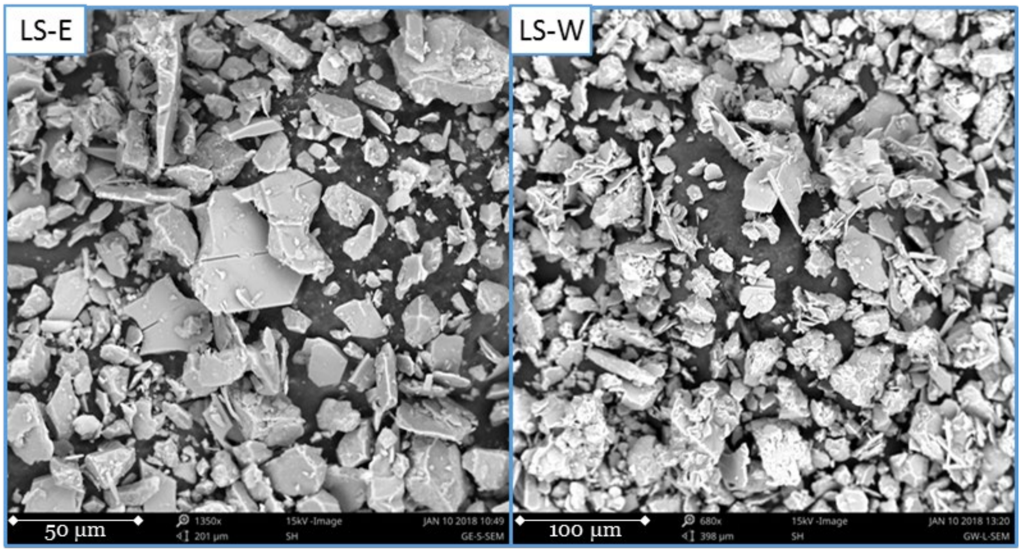

Figure 27. Average dust-emission fluxes (mg m^{-2} s^{-1}) for all large-scale test plots measured by PI-SWERL.

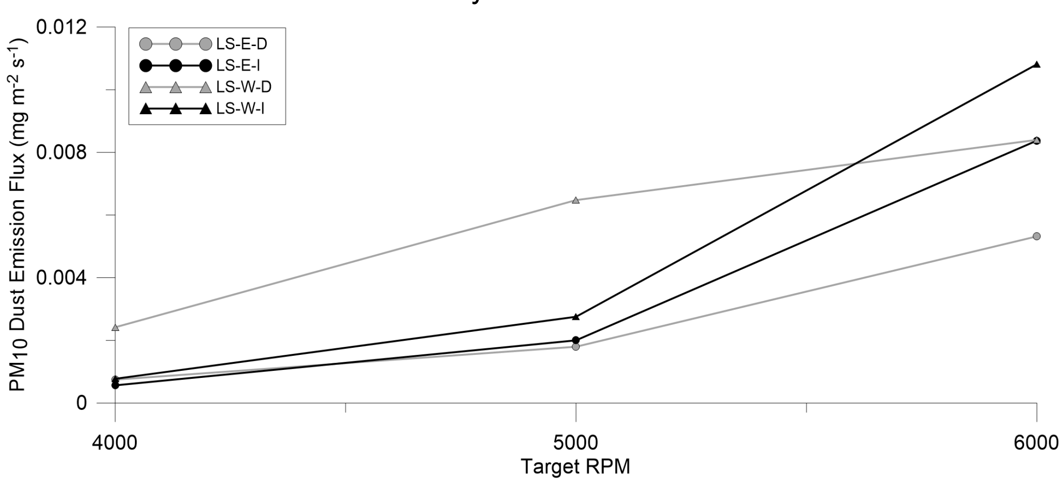

The most interesting result from our dust-emission potential assessment was that the highest PM10 fluxes were from MS-2, MS-4, and MS-6. All of these plots were misted plots, two were heated inside of a tent, and the other was exposed to the ambient conditions of the study environment. The dust fluxes from all three of these plots, though low, were an order of magnitude greater than the other groundwater-fed plots. Interestingly, the high fluxes in MS-2 and MS-6 were from an area of the plot with indirect lighting, whereas MS-4 was sampled from directly heated locations. It is also important to note that MS-6 produced higher dust-emission fluxes regardless of the heat-lamp proximity.

There is a possibility that dust created by other activities in the facility may have deposited on the surface of MS-6, leading to higher dust-emission potential. However, if this were the case, we would expect higher emissions from MS-5 (the other nonenclosed plot) as well, which did not occur. Some salt evaporites developed on all of the plot surfaces (as evidenced by the SEM analysis and daily photos taken to document crust formation). These evaporites may have contributed to the overall PM10 concentrations measured by the PI-SWERL, but there were no physical markers in the imagery that would suggest that salt evaporites were the sole cause of these emission disparities. These higher fluxes could also be a result of abrasion caused by detached crust edge pieces during testing. We believe this was the driving mechanism for our highest measured dust-emission flux average, which occurred in MS-4. A centimeter-scale section of crust appeared to have broken free during a PI-SWERL test and produced so much dust that it surpassed the monitoring capability of the PI-SWERL instrument at 5800 rpm.

We believe that differences in surface-crust moisture content explain the variability observed in our dust-emission flux measurements. Soil water suction forces, matric potential, can markedly reduce dust-emission onset and magnitude (McKenna-Neuman and Nickling 1989; Fécan et al. 1999). According to Fécan et al. (1999), the effects of suction on the amount of shear stress needed to mobilize a soil particle can be quantified via

$$f(w) = \begin{cases} \sqrt{1 + A(w - w')^{b'}}, & w > w' \\ 1, & w \leq w' \end{cases}$$

$$w' = 0.0014c^2 + 0.17c,$$

where

A = 1.21,
b' = 0.68,
w = the gravimetric soil-moisture content, and
c = the soil clay composition percentage.

Following this approach, suction forces were likely suppressing dust emission in plots with crust moisture contents exceeding 2%.

Table 13 provides the average measured gravimetric soil-moisture contents for plot crusts and their corresponding $f(w)$ estimates. Meter-scale plots MS-2, MS-4, and MS-6 all had crust gravimetric moisture content averages near or less than 1%. MS-6 had moisture content averages of 1.0% and 2.6% for direct and indirect lighting, respectively. We would have expected these values to be higher than MS-2 and MS-4 given that this plot did not have ambient heat control. The groundwater-fed meter-scale plots had much higher gravimetric moisture content averages ranging from 7.9% to 12.1%, with most values under 10%. The large-scale plot had the wettest surface crust at 12.6% to 13.9% moisture content and also exhibited the lowest dust-emission flux. These data suggest that, although we allowed a week for drying, the groundwater-fed soil packages were still wicking water to the immediate soil surface while in-plot samples were being collected.

Table 13. Percent moisture content of surface-crust samples taken from large- and meter-scale plots.

Tenting	Plot #	Lighting	Water Feed	f(w)	Moisture (%)	SD (%)
Tent #1	MS-1	Direct	Groundwater	2.4	9.2	0.43
	MS-1	Indirect	Groundwater	2.4	10.1	0.50
	MS-2	Direct	Misted	1.0	0.1	0.02
	MS-2	Indirect	Misted	1.0	0.2	0.05
Tent #2	MS-3	Direct	Groundwater	2.2	7.9	0.72
	MS-3	Indirect	Groundwater	2.3	8.8	0.77
	MS-4	Direct	Misted	1.0	0.1	0.10
	MS-4	Indirect	Misted	1.3	1.4	0.97
Ambient	MS-5	Direct	Groundwater	2.6	8.4	0.75
	MS-5	Indirect	Groundwater	1.0	12.1	2.08
	MS-6	Direct	Misted	1.3	1.0	0.14
	MS-6	Indirect	Misted	2.6	2.6	0.36
Greenhouse	LS-West	Direct	Groundwater	2.7	12.6	1.13
	LS-West	Indirect	Groundwater	2.7	13.9	0.68
	LS-East	Direct	Groundwater	2.7	13.5	0.24
	LS-East	Indirect	Groundwater	2.7	13.6	0.07

Our physical crust data assessments produced fewer significant trends than our chemistry analyses. Following a Box-Cox transformation, we performed a PCA to determine if there were any correlations between the samples or treatments (Figure 28). The PCA results did not show any clear differentiation between treatments. However, one-way ANOVA tests based on saltwater-delivery mechanism suggest there are significant differences between crusts created by misting and the groundwater-delivery methods (Figure 29). Specifically, groundwater-fed crusts were thicker with a greater shear strength.

Figure 28. Results of the principal component analysis of physical crust data (MS = meter-scale, LS = large-scale, GW = groundwater, SM = misted, D = direct lighting, and I = indirect lighting).

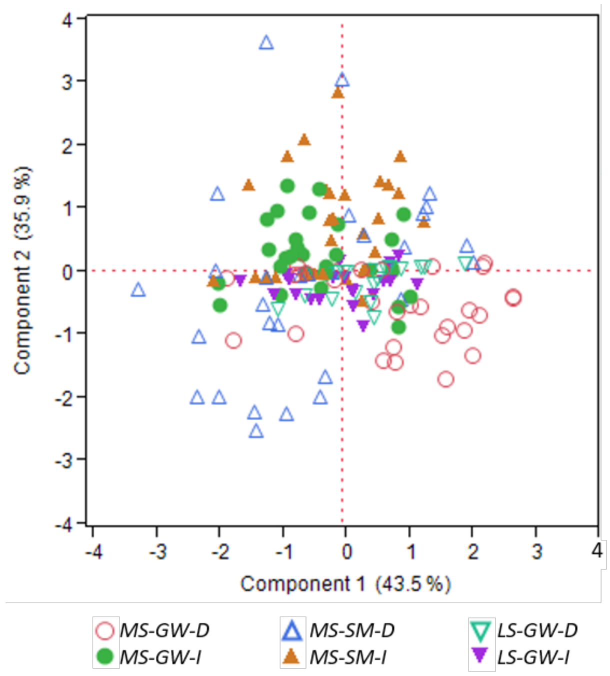

Figure 29. Results of the one-way ANOVA test of transformed compressive strength, shear strength, and crust thickness data based on saltwater-delivery method (GW = groundwater, and SM = misted).

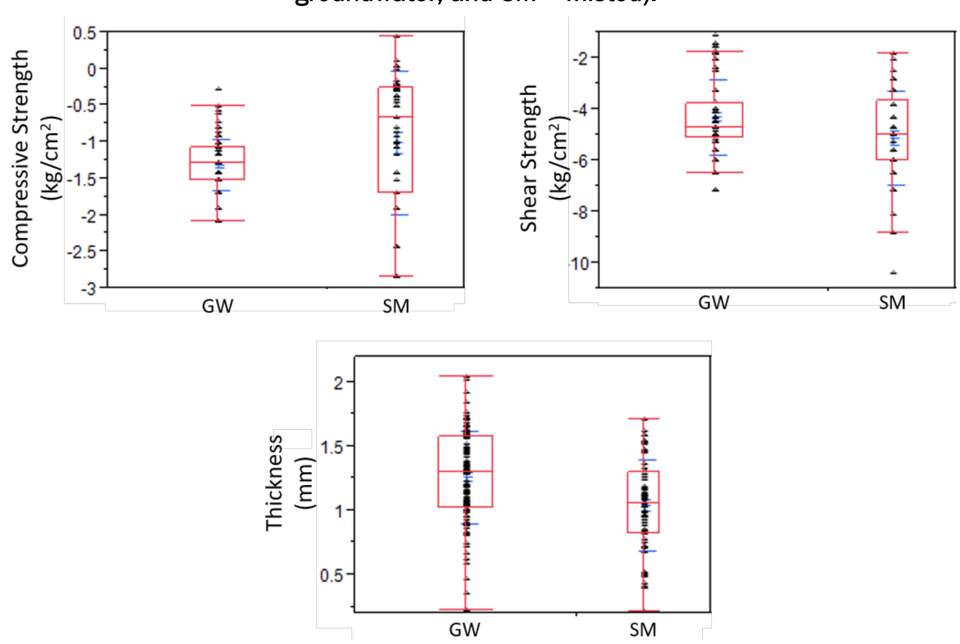

Further investigation of other factors (e.g., sampling location and TDS of saltwater), however, did not indicate a significant difference between misted- and groundwater-fed plots (Figure 30). Based on these analyses, we believe that saltwater-delivery method (misted or groundwater) does have a significant effect on the physical characteristics of resultant soil crusts; however, effects due to heat-lamp placement and salt concentration on crust formation require further investigation.

Figure 30. Results of the one-way ANOVA test of transformed physical crust data based on delivery method, lighting, and TDS of feed water (D = direct lighting, I = indirect lighting, GW = groundwater, SM = misted, 10k = 10,000 ppm TDS, 5k = 5000 ppm TDS).

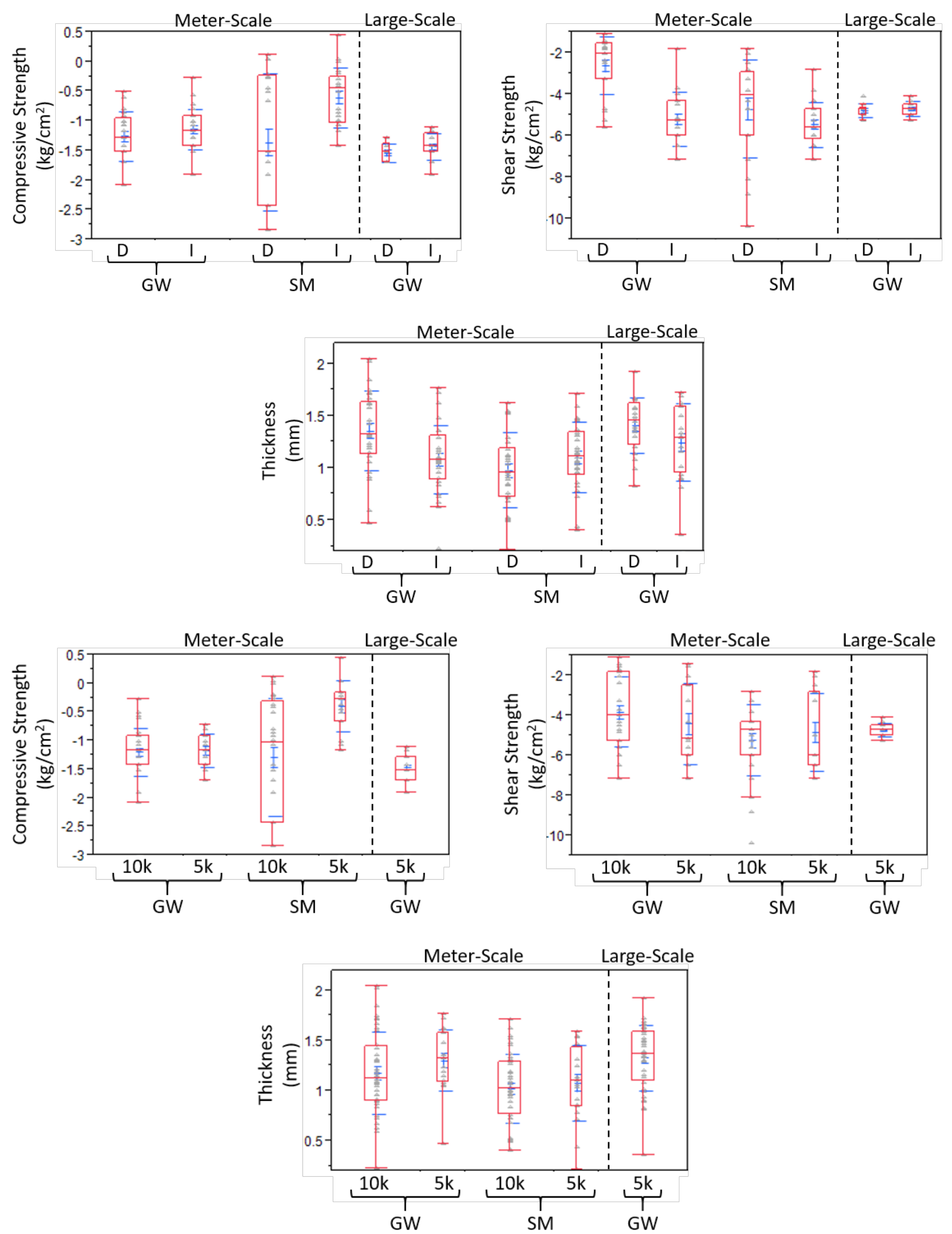

3.5 Real-world comparison

We then compared our simulated plot results to those obtained from real-world playas. Examples of playa include Franklin Lake Playa at 36.254, −116.371 (Goldstein et al. 2011); Salton Sea (playa-like) at 33.497, −116.0798 (King et al. 2011; Sweeney et al. 2011); Mesquite Lake at 35.714, −115.598 (Sweeney et al. 2011); and Soda Lake at 35.126, −116.111 (Sweeney et al. 2011). Unfortunately, we were unable to find enough common types of measurements in the literature for robust statistical comparisons. As such, we were able to do only qualitative analyses to assess whether our results are within the range of measurements taken from the field.

Physical crust attribute comparisons between our simulated crusts (e.g., Table 11 and Table 12) with those measured from Franklin Lake Playa (Table 14) suggest our manually created crusts exhibit realistic compressive strength characteristics.

Table 14. Average physical crust data from this study and from Goldstein et al. 2011, which measured over the course of 3–4 years, depending on sample location.

Location	Compressive Strength (kg/cm^2)	Compressive Strength (std dev)	Shear Strength (kg/cm^2)	Shear Strength (std dev)	Thickness (mm)	Thickness (std dev)
Meter-scale—Water Table	0.30	0.13	0.11	0.10	3.46	1.24
Meter-scale—Misted	0.49	0.38	0.06	0.05	2.90	0.94
Large-scale—Water Table	0.21	0.05	0.05	0.01	3.76	1.05
Discovery Repeat Site 1	0.83	1.39	1.93	2.61	-	-
East Transect Repeat Site 1	1.26	0.98	1.39	0.64	-	-
West Transect Repeat Site 1	4.08	1.00	5.92	0.64	-	-
Discovery Repeat Site	0.25	1.00	-	-	9.09	2.55
East Transect Repeat Site	0.81	0.99	-	-	16.98	4.73
West Transect Repeat Site	2.79	0.96	-	-	14.58	5.28

There is an order of magnitude difference between the crust thicknesses and shear strengths of the simulated and Franklin Lake Playa crusts. However, the RSDs of the Franklin Lake Playa data are similar to those of the simulated crusts. Given that our formation period was limited to 8 weeks (plus one week for drying), we may have been able to produce a thicker crust had we allowed the evolution period to go on for a longer duration.

Dust-emission flux measurements by King et al. (2011) and Sweeney et al. (2011) were collected under shear velocities on the order of 0.56 m s^{-1}, which is roughly comparable to a 3000 rpm fan speed on the PI-SWERL.

Although our lowest fan speed measurements were collected at 4000 rpm (shear velocity of ~0.72 m s^{-1}), our 4000 rpm dust-emission flux data are on the same order of magnitude as those measured by King et al. (2011) (Table 15).

Table 15. Summary of mean dust-emission potential (mg m^{-2} s^{-1}) and standard deviations for playa-like conditions around the Salton Sea (adapted from King et al. 2011 data). These data were measured at a shear velocity of 0.56 m s^{-1}.

Site	September 2006		January 2007		March 2007		February 2008	
	Mean	σ	Mean	σ	Mean	σ	Mean	σ
PL-1							0.262	1.993
PL-2							0.019	2.130
PL-4	0.006	1.478	0.150	1.903			0.087	1.736
PL-5	0.013	3.443	0.026	3.184	0.003	1.437	0.030	1.301
PL-6	0.004	2.650						
PL-7			1.426	3.290			0.179	3.048
PL-8			0.107	1.908			0.901	1.666
PL-9			0.239	5.546			0.011	1.749
PL-10	0.005	3.481	0.359	1.942	0.006	1.116	0.008	1.301
PL-11	0.034	4.143	2.459	1.137	0.017	5.200		
PL-12	0.008	2.763	0.060	1.476	0.202	3.013	0.011	1.696

Sweeney et al. (2011) assessed the average dust-emission flux value for 54 measured locations on salt-playa surfaces. The maximum value was 0.6923 mg m^{-2} s^{-1}, and the minimum was 0.0019 mg m^{-2} s^{-1}. The minimum flux measured by Sweeney et al. (2011) is the same order of magnitude as the fluxes from the simulated playa surfaces in this study, with the average fluxes from the meter- and large-scale plots being 0.0109 and 0.0011 mg m^2 s^{-1} at 4000 rpm, respectively.

The overlap in values for the dust-emission flux measurements from our plots and those measured in situ by King et al. (2011) and Sweeney et al. (2011) provide some confidence that our artificial crusts have similar attributes to those found in the real world. Had we allowed more time for development, longer drying periods, and (in the case of the groundwater-fed plots) drained the groundwater source between the evolution and drying phases, our artificial playa surfaces may have been more similar to the real-world analogs.

4 Conclusions

4.1 Saltwater-delivery methods

Based on our investigation, it is clear that both the misted and groundwater saltwater-delivery methods can be used to create playa-like, salt-crusted soil surfaces. However, characteristics of crusts created by the two methods may be markedly different. In general, the groundwater saltwater-delivery system created thicker crusts with higher shear strength. Groundwater-produced crusts also experienced significantly more surface cracking during the course of the experiment than the misted plots, most likely due to expansion of the soil package when saltwater was added from below. Chemical compositions of the simulated crusts were highly dependent on the saltwater-delivery method. Crust pH was identified as varying most significantly between the groundwater-fed and misted plots, which likely was caused by varied precipitation of applied bicarbonate.

These results indicate that the choice of saltwater-delivery method should be based on the resultant crust attributes needed for the final test space. Crusts produced via the groundwater-delivery method were generally less sensitive to variations in saltwater concentration due to the filtering action of the soil package. This approach to groundwater delivery may be more robust to environmental influences and therefore easier to replicate in subsequent experiments.

4.2 Salinity variation

Statistically significant variations in crust salinity were identified from dissolved ion levels. Crusts created via the groundwater-delivery method had higher levels of dissolved ions. This is most likely due to the high volume of saltwater required for the groundwater method to work. Groundwater systems required about five times the amount of saltwater compared to the misted boxes and, therefore, developed higher salt contents at the plot surface through evaporative processes.

4.3 Climate control

Climate-control systems did not have a discernable effect on soil-moisture levels in the groundwater-fed plots. However, direct and indirect lighting had a significant effect on specific crust traits. The large-scale test plot was also much slower to generate a crust than the meter-scale test plots, even though the large-scale system had lower relative humidity and higher overall air temperatures. We believe that heat exposure along the sides of the soil package was an important factor. This was the only functional difference between the meter-scale and large-scale test plots (above ground boxes versus an in-ground plot) with regard to climate control.

4.4 Crust characteristics

Physical crust measurements did differ between crusts created by the two saltwater-delivery methods. Groundwater-fed crusts tended to have higher moisture content, be thicker, and have higher shear strength, whereas the misted crusts tended to have higher compressive strength. When comparing physical crust characteristics to real-world analogs, there was some overlap in the compressive strengths of the crusts, but not with shear strength or thickness. A longer timeframe for crust creation is likely needed to generate crusts more structurally and physically similar to real-world analogs.

Overall dust-emission flux was greater from misted plots, which was likely the result of higher crust water content in the groundwater-fed plots. The misted plots produced dust-emission fluxes, although on the lower end, similar to dust-emission fluxes collected from real-world analogs found in the southwestern United States. With additional time for crust drying and removal of the capillary water connection (i.e., draining the groundwater) between the evolution and drying phases, dust-emission fluxes from our simulated plots could potentially increase and measure closer to those in nature.

5 Recommendations

Our investigation brought to light several phenomena that should be considered when simulating a crust on meter to larger scales.

The surface heating method for the plot should be distributed as evenly as possible. When using direct lighting or surface application of heat, we found a distinct difference (visually and topographically) between sections of the plot that had direct heat application and those that did not. To remedy this issue, we suggest the use of infrared heating panels. This alternate approach may better distribute heat over the entire surface and remove the direct versus indirect heat-lamp-exposure variable.

The soil temperatures in the large-scale test plot tended to be much lower than those in the meter-scale test plots. To address this and to conform with the even heat distribution described above, we suggest using infrared heating panels over large testing surfaces and the addition of subsurface heating panels that could combat the heat sink of surrounding construction materials (e.g., concrete, nonheated soil, etc.). Use of subsurface panels (and additional surface insulation) could also potentially allow crust formation year-round in areas prone to extreme cold conditions.

The moisture delivery of the larger-scale test plot should also be adjusted for even distribution of saltwater throughout the artificial groundwater source. Our design used a sump in case the groundwater needed to be drained. This caused the water to stay pitched toward the southeastern corner of the plot, therefore allowing water to reach the surface much quicker in the southeastern corner than the northwestern corner. We suggest using a two-point delivery system, dividing the subsurface into two pitched halves in opposite directions. This would allow water to wick to the surface quickly at both ends and toward the middle last. Another potential solution for this issue could be the use of a level artificial groundwater source, but this would not allow for rapid drainage.

Finally, we suggest reducing the volume of and better insulating the air space above the plot surface to increase the effectiveness of the climate-control system and to reduce energy costs. Lowering the height of the air space, however, should be balanced with plot accessibility needs for crust evolution monitoring and misted saltwater application.

Further research is needed to better understand processes governing spatial and temporal variations of emissions from aeolian (wind-driven) and fugitive (disturbance-induced) dust sources (such as dust produced by downwash from rotorcraft or surface shear from tires), especially on playa or playa-like surfaces important for mobility applications. This report evaluated methods for replicating salt-crusted playa surface conditions on soil plots large enough to support applications like vehicular dust-emission testing. Although opportunity for further refining these approaches remains, our results suggest the techniques discussed in this report can create representative surface conditions for dust-emission experimentation in a controlled environment.

References

AMS, Inc. 2018. *Part #59035 GeoTester Penetrometer*. Technical Data Sheet. American Falls, ID: AMS, Inc. https://www.ams-samplers.com/pub/pdfs/ams-Geotester-Without-Price.pdf.

ASTM International. 2017. *Standard Test Method for Particle-Size Distribution (Gradation) of Fine-Grained Soils Using the Sedimentation (Hydrometer) Analysis*. ASTM D7928-17. West Conshohocken, PA: ASTM International. https://doi.org/10.1520/D7928-17.

Box, G. E. P., and D. R. Cox. 1964. "An Analysis of Transformations." *Journal of the Royal Statistical Society: Series B (Methodological)* 26 (2): 211–252.

Bullard, J. E., M. Baddock, T. Bradwell, J. Crusius, E. Darlington, D. Gaiero, S. Gassó, G. Gisladottir, R. Hodgkins, R. McCulloch, C. McKenna-Neuman, T. Mockford, H. Stewart, and T. Thorsteinsson. 2016. "High-Latitude Dust in the Earth System." *Reviews of Geophysics* 54 (2): 447–485. https://doi.org/10.1002/2016RG000518.

CRREL (Cold Regions Research and Engineering Laboratory). 2018. "Frost Effects Research Facility: Year-Round, Reliable Testing of Frost Effects." Engineer Research and Development Center. http://www.erdc.usace.army.mil/Media/FactSheets/FactSheetArticleView/tabid/9254/Article/476644/frost-effects-research-facility.aspx.

Dean, W., Jr. 1974. "Determination of Carbonate and Organic Matter in Calcareous Sediments and Sedimentary Rocks by Loss on Ignition: Comparison with Other Methods." *SEPM Journal of Sedimentary Research* 44 (1): 242–248. https://doi.org/10.1306/74D729D2-2B21-11D7-8648000102C1865D.

Department of Defense. 1964. *Subgrade, Subbase, and Test Method for Pavement Base-Course Materials*. Revision A. MIL-STD-621A. Washington, DC: Department of Defense.

Desert Studies Center. 2015. "About Soda Springs." The California State University Desert Studies Center. Fullerton, CA: College of Natural Sciences and Mathematics, California State University. http://nsm.fullerton.edu/dsc/desert-studies-about (accessed 9 April 2018).

Etyemezian, V., G. Nikolich, S. Ahonen, M. Pitchford, M. Sweeney, R. Purcell, J. Gillies, and H. Kuhns. 2007. "The Portable In Situ Wind Erosion Laboratory (PI-SWERL): A New Method to Measure PM10 Windblown Dust Properties and Potential for Emissions." *Atmospheric Environment* 41 (18): 3789–3796. https://doi.org/10.1016/j.atmosenv.2007.01.018.

Fécan, F., B. Marticorena, and G. Bergametti. 1999. "Parametrization of the Increase of the Aeolian Erosion Threshold Wind Friction Velocity Due to Soil Moisture for Arid and Semi-Arid Areas." *Annales Geophysicae* 17:149–157.

Goldstein, H. L., G. N. Breit, J. C. Yount, R. L. Reynolds, M. C. Reheis, G. L. Skipp, E. M. Fisher, and P. J. Lamothe. 2011. *Physical, Chemical, and Mineralogical Data from Surficial Deposits, Groundwater Levels, and Water Composition in the Area of Franklin Lake Playa and Ash Meadows, California and Nevada*. Data Series 607. Reston, VA: U.S. Geological Survey.

Goldstein, H. L., G. N. Breit, and R. L. Reynolds. 2017. "Controls on the Chemical Composition of Saline Surface Crusts and Emitted Dust from a Wet Playa in the Mojave Desert (USA)." *Journal of Arid Environments* 140 (May): 50–66. https://doi.org/10.1016/j.jaridenv.2017.01.010.

Hillel, D. 1982. *Introduction to Soil Physics*. San Diego: Academic Press.

King, J., V. Etyemezian, M. Sweeney, B. J. Buck, and G. Nikolich. 2011. "Dust Emission Variability at the Salton Sea, California, USA." *Aeolian Research* 3 (1): 67–79. https://doi.org/10.1016/j.aeolia.2011.03.005.

Langston, G., and C. McKenna-Neuman. 2005. "An Experimental Study on the Susceptibility of Crusted Surfaces to Wind Erosion: A Comparison of the Strength Properties of Biotic and Salt Crusts." *Geomorphology* 72 (1–4): 40–53. https://doi.org/10.1016/j.geomorph.2005.05.003.

McKenna-Neuman, C., and W. G. Nickling. 1989. "A Theoretical and Wind Tunnel Investigation of the Effect of Capillary Water on the Entrainment of Sediment by Wind." *Canadian Journal of Soil Science* 69 (1): 79–96. https://doi.org/10.4141/cjss89-008.

Natural Resources Conservation Service. n.d. "Area of Interest (AOI)." U.S. Department of Agriculture, Natural Resources Conservation Service, Web Soil Survey. https://websoilsurvey.sc.egov.usda.gov/App/WebSoilSurvey.aspx.

———. 2015. "Web Soil Survey Home." U.S. Department of Agriculture, Natural Resources Conservation Service, Web Soil Survey. https://websoilsurvey.sc.egov.usda.gov/ (accessed 29 December 2015).

Nield, J. M., C. McKenna-Neuman, P. O'Brien, R. G. Bryant, and G. F. S. Wiggs. 2016. "Evaporative Sodium Salt Crust Development and Its Wind Tunnel Derived Transport Dynamics under Variable Climatic Conditions." *Aeolian Research* 23 (December): 51–62. https://doi.org/10.1016/j.aeolia.2016.09.003.

Prospero, J. M. 2002. "Environmental Characterization of Global Sources of Atmospheric Soil Dust Identified with the NIMBUS 7 Total Ozone Mapping Spectrometer (TOMS) Absorbing Aerosol Product." *Reviews of Geophysics* 40 (1). https://doi.org/10.1029/2000RG000095.

Reynolds, R. L., J. C. Yount, M. Reheis, H. Goldstein, P. Chavez, R. Fulton, J. Whitney, C. Fuller, and R. M. Forester. 2007. "Dust Emission from Wet and Dry Playas in the Mojave Desert, USA." *Earth Surface Processes and Landforms* 32 (12): 1811–1827. https://doi.org/10.1002/esp.1515.

Rosen, M. R. 1994. "The Importance of Groundwater in Playas: A Review of Playa Classifications and the Sedimentology and Hydrology of Playas." In *Paleoclimate and Basin Evolution of Playa Systems*, 289:1–18. McLean, VA: Geological Society of America. https://doi.org/10.1130/SPE289-p1.

Soil Science Division Staff. 2017. *Soil Survey Manual*. Agriculture Handbook 18. Washington, DC: Government Printing Office.

Sweeney, M. R., E. V. McDonald, and V. Etyemezian. 2011. "Quantifying Dust Emissions from Desert Landforms, Eastern Mojave Desert, USA." *Geomorphology* 135 (1–2): 21–34. https://doi.org/10.1016/j.geomorph.2011.07.022.

Sweeney, M. R., E. V. McDonald, and C. E. Markley. 2013. "Alluvial Sediment or Playas: What Is the Dominant Source of Sand and Silt in Desert Soil Vesicular A Horizons, Southwest USA." *Journal of Geophysical Research: Earth Surface* 118 (1): 257–75. https://doi.org/10.1002/jgrf.20030.

Tukey, J. W. 1949. "Comparing Individual Means in the Analysis of Variance." *Biometrics* 5 (2): 99. https://doi.org/10.2307/3001913.

Ward, J. H. 1963. "Hierarchical Grouping to Optimize an Objective Function." *Journal of the American Statistical Association* 58 (301): 236. https://doi.org/10.2307/2282967.

Appendix A: Real-World Playa Soil Texture Data

Table A-1. Textural and location data for playas from Sweeney et al. (2013)

Location	Sample ID	%Sand	%Silt	%Clay
Mojave	SV1	26.2	46.7	27.2
	SV2	27	46.2	26.7
	SV3	24.9	47.6	27.4
	SV4	23.5	45.7	30.7
	SV5	26.2	42.2	31.4
	SV6	32	36.7	31.4
	SV7	38.8	29.9	31.3
	SV8	34.6	31.5	33.9
	SV9	29	63.1	8
	SLW-1	50.9	38.5	10.6
	SLW-3	63.4	30.6	6
	SLW-5	60.9	32.4	6.7
	SLW-6	11.9	64.9	23.1
	SLW-8	34.6	58.3	7
	SLC-1	18.7	71.1	10.2
	SLC-3	20.5	68.4	11.2
	SLC-5	7	73	20
	SLC-7	11.7	65.2	23
	SLC-9	10.7	65.6	23.7
	SLE-1	25.2	60.4	14.4
	SLE-3	33.1	52.9	14
	SLE-5	13.9	54.3	31.8
	SLE-7	30.8	36.5	32.7
Sonoran	SS17	3.3	44	52.7
	A31	7.5	47.7	44.8
	A32	9.2	64.6	26.3
	A34	86.2	9.2	4.6
	A101	6.8	52.4	40.8
	PAT5	12.5	56.3	31.3

Table A-2. Textural and location data from the Web Soil Survey (Natural Resources Conservation Service, n.d.).

Sample ID	Latitude	Longitude	%Sand	%Silt	%Clay
Unnamed_Playa_01	38.484293	−115.6712	2.5	42.5	55
Unnamed_Playa_03	35.722134	−115.5862	65	28	7
Unnamed_Playa_12	34.322206	−109.8705	5.3	44.7	50
Unnamed_Playa_13	32.257328	−109.7971	65.9	19.1	15
Unnamed_Playa_14	32.22499	−109.8279	44.3	40.7	15
Unnamed_Playa_15	32.145079	−109.8450	65.9	19.1	15
Unnamed_Playa_16	32.296331	−108.9022	3.1	44.4	52.5
Unnamed_Playa_17	33.827309	−108.1914	5.3	44.7	50
Bicycle Lake Airfield	35.276301	−116.6308	6.8	63.2	30

Figure A-1. Ternary diagram of texture data used for comparison to our study soil. *Red triangles* are from Web Soil Survey (Table A-2); *green diamonds* and *orange squares* are from the Sonoran and Mojave Deserts (Sweeney et al. 2013); *blue circles* are our study soil.

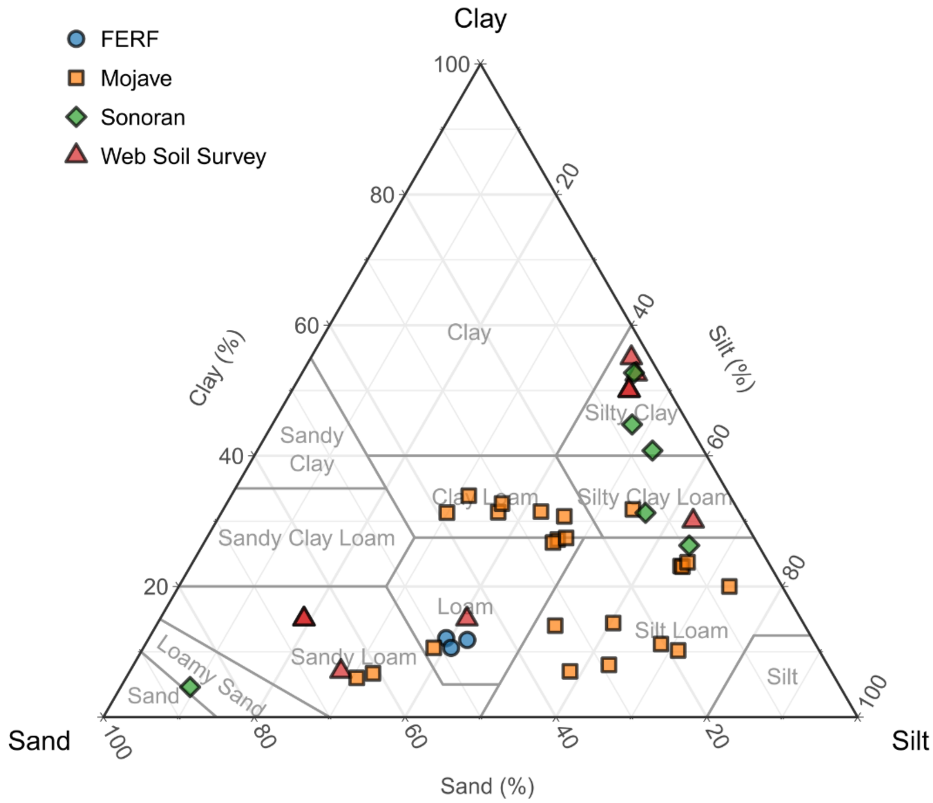

Table A-3. Water chemistry results for saltwater solution used throughout our study.

Sample ID	Date Sampled	pH	Alkalinity (mg as $CaCO_3$ L^{-1})	Concentration (mg/kg)							
				Na^+	K^+	Mg^{2+}	Ca^{2+}	Cl^-	SO_4^{2-}	NO_3^-	PO_4^{3-}
FERF-50-5K-001	8/17/2017	8.12	305	1178	81	212	361	2170	806	<10	<10
FERF-50-5K-002	9/7/2017	-	-	1174	72	205	352	2153	803	<10	<10
FERF-50-5K-003	9/8/2017	-	-	1170	72	208	360	2168	809	<10	<10
FERF-50-5K-004	9/12/2017	-	-	1191	73	212	358	2217	826	<10	<10
FERF-50-5K-005	9/14/2017	-	-	1173	71	211	355	2199	816	<10	<10
FERF-50-5K-006	9/18/2017	-	-	1155	52	207	348	2173	812	<10	<10
FERF-50-5K-007	9/20/2017	-	-	1183	70	213	370	2236	832	<10	<10
FERF-50-5K-008	9/22/2017	8.08	329	1191	71	214	366	2234	834	<10	<10
FERF-50-5K-009	9/26/2017	-	-	1168	70	210	361	2187	813	<10	<10
FERF-50-5K-010	9/29/2017	-	-	1186	70	214	373	2223	836	<10	<10
FERF-50-5K-011	10/3/2017	-	-	1167	69	211	361	2192	826	<10	<10
FERF-50-5K-012	10/10/2017	-	-	1140	68	211	360	2199	823	<10	<10
FERF-50-5K-013	10/13/2017	-	-	1178	69	211	363	2212	826	<10	<10
FERF-50-5K-014	10/19/2017	-	-	1173	68	209	362	2194	822	<10	<10
FERF-50-5K-015	10/24/2017	8.05	316	1161	68	208	361	2192	817	<10	<10
FERF-1K-5K-001	8/15/2017	8.11	319	1145	75	206	344	2177	810	<10	<10
FERF-1K-5K-002	9/7/2017	-	-	1111	57	192	326	2200	819	<10	<10
FERF-1K-5K-003	9/8/2017	-	-	1163	62	203	346	2191	817	<10	<10
FERF-1K-5K-004	9/12/2017	-	-	1157	69	205	343	2209	821	<10	<10
FERF-1K-5K-005	9/15/2017	8.09	313	1165	65	207	343	2235	824	<10	<10
FERF-1K-5K-006	9/21/2017	-	-	1172	72	209	347	2222	827	<10	<10
FERF-1K-5K-007	9/27/2017	-	-	1244	78	223	367	2355	875	<10	<10
FERF-1K-5K-008	10/6/2017	-	-	1174	73	210	356	2219	826	<10	<10
FERF-1K-5K-009	10/19/2017	8.38	319	1171	73	209	345	2217	796	<10	<10
FERF-50-10K-001	8/17/2017	-	-	2241	139	400	645	4252	1594	<20	<20
FERF-50-10K-002	9/6/2017	-	-	2267	164	411	679	4319	1634	<20	<20
FERF-50-10K-003	9/7/2017	-	-	2672	157	480	746	5161	1901	<20	<20
FERF-50-10K-004	9/8/2017	8.03	586	2260	136	413	689	4431	1675	<20	<20
FERF-50-10K-005	9/11/2017	-	-	2264	137	403	666	4303	1618	<20	<20
FERF-50-10K-006	9/12/2017	-	-	2291	137	411	676	4354	1639	<20	<20
FERF-50-10K-007	9/13/2017	-	-	2281	137	405	675	4382	1642	<20	<20
FERF-50-10K-008	9/14/2017	-	-	2294	125	403	666	4372	1636	<20	<20
FERF-50-10K-009	9/15/2017	-	-	2336	141	416	692	4474	1674	<20	<20
FERF-50-10K-010	9/18/2017	8.23	593	2255	136	399	672	4309	1616	<20	<20
FERF-50-10K-011	9/19/2017	-	-	2296	142	407	662	4410	1649	<20	<20
FERF-50-10K-012	9/20/2017	-	-	2278	163	407	672	4313	1624	<20	<20
FERF-50-10K-013	9/21/2017	-	-	2195	130	400	646	4318	1622	<20	<20
FERF-50-10K-014	9/22/2017	-	-	2355	137	420	689	4495	1688	<20	<20
FERF-50-10K-015	9/25/2017	-	-	2016	109	352	587	3835	1441	<20	<20
FERF-50-10K-016	9/26/2017	-	-	2273	137	401	666	4332	1626	<20	<20

Table A-3 (cont.). Water chemistry results for saltwater solution used throughout our study.

Sample ID	Date Sampled	pH	Alkalinity (mg as $CaCO_3$ L^{-1})	Concentration (mg/kg)							
				Na^+	K^+	Mg^{2+}	Ca^{2+}	Cl^-	SO_4^{2-}	NO_3^-	PO_4^{3-}
FERF-50-10K-017	9/27/2017	-	-	2270	139	418	715	4477	1678	<20	<20
FERF-50-10K-018	9/28/2017	-	-	2260	136	415	693	4506	1700	<20	<20
FERF-50-10K-019	10/2/2017	-	-	2244	138	410	659	4374	1652	<20	<20
FERF-50-10K-020	10/3/2017	7.97	589	2263	138	413	674	4399	1656	<20	<20
FERF-50-10K-021	10/5/2017	-	-	2226	136	405	631	4361	1631	<20	<20
FERF-50-10K-022	10/10/2017	-	-	2247	147	409	654	4402	1653	<20	<20
FERF-50-10K-023	10/11/2017	-	-	2260	118	396	632	4315	1618	<20	<20
FERF-50-10K-024	10/16/2017	-	-	2269	128	401	612	4309	1613	<20	<20
FERF-50-10K-025	10/17/2017	-	-	2258	131	411	653	5122	1928	<20	<20
FERF-50-10K-026	10/19/2017	-	-	2275	129	404	666	4360	1639	<20	<20
FERF-50-10K-027	10/24/2017	-	-	2199	126	389	620	4184	1570	<20	<20
FERF-50-10K-028	10/26/2017	-	-	1985	119	358	591	3861	1449	<20	<20
FERF-1K-Pre-Mix	8/15/2017	-	-	11.6	1.39	1.03	10.6	14.1	5.1	<0.1	2.4

Appendix B: Simulated Crust Chemistry Data

Table B-1. Full chemical dataset for simulated crust samples.

Sample ID	Moisture (wt %)	1:5 Deionized Water Extraction		Dissolved Ions from 1:5 Extraction (mg/kg dry sample)							
		pH	EC (mS/cm)	Na^{+}	K^{+}	Mg^{+2}	Ca^{+2}	Cl^{-}	SO_4^{-2}	NO_3^{-}	PO_4^{-}
MS-1-S-CHEM-01	9.5	7.83	46.28	29547	48	1258	18084	81405	14072	2141	<600
MS-1-S-CHEM-02	10.4	7.9	34.87	17566	25	1148	15917	55599	15108	1890	<600
MS-1-S-CHEM-03	10.4	7.91	40.91	22463	32	1310	17966	67168	16657	2508	<600
MS-1-L-CHEM-01	8.7	7.74	46.77	25955	68	1130	19728	81726	8549	2333	<600
MS-1-L-CHEM-02	9.5	7.84	45.54	23616	52	778	19935	77253	7950	3632	<600
MS-1-L-CHEM-03	9.3	7.72	50.3	12223	58	1211	31650	90251	1130	5054	<600
MS-2-S-CHEM-01	0.2	8.73	0.8587	285	3	39	196	518	932	<60	<60
MS-2-S-CHEM-02	0.3	8.69	1.387	446	4	60	544	846	1962	<60	<60
MS-2-S-CHEM-03	0.3	8.6	1.11	446	2	27	250	742	1331	<60	<60
MS-2-L-CHEM-01	0.1	8.96	0.8947	356	3	47	185	708	826	<60	<60
MS-2-L-CHEM-02	0.1	8.92	0.68	274	2	22	141	508	593	<60	<60
MS-2-L-CHEM-03	0.1	8.89	0.972	398	4	42	171	827	725	<60	<60
MS-3-S-CHEM-01	9.6	8.04	52.46	37288	37	1267	16597	91128	15712	1528	<600
MS-3-S-CHEM-02	8.6	7.94	71.08	57955	44	1491	17376	128316	14568	1946	<600
MS-3-S-CHEM-03	8.1	7.95	70.55	58197	42	1491	16836	127241	13846	1893	<600
MS-3-L-CHEM-01	7.8	7.94	74.38	53786	100	2055	23742	141833	5596	2085	<600
MS-3-L-CHEM-02	8.7	7.94	77.9	58483	96	1486	24066	151633	3914	1412	<600
MS-3-L-CHEM-03	7.3	8.12	64.29	29941	128	2575	33285	100675	2602	933	<600
MS-4-S-CHEM-01	0.6	8.64	4.65	2640	13	263	2494	5403	7237	<60	<60
MS-4-S-CHEM-02	1.0	8.87	5.814	2176	13	256	3747	4420	10829	<60	<60
MS-4-S-CHEM-03	2.5	8.79	7.244	3275	17	385	3316	6754	9564	<60	<60
MS-4-L-CHEM-01	0.1	9.6	7.201	4639	30	380	1176	8827	3873	<60	<60

Table B-1 (cont.). Full chemical dataset for simulated crust samples.

Sample ID	Moisture (wt %)	1:5 Deionized Water Extraction		Dissolved Ions from 1:5 Extraction (mg/kg dry sample)							
		pH	EC (mS/cm)	Na^{+}	K^{+}	Mg^{+2}	Ca^{+2}	Cl^{-}	SO_4^{-2}	NO_3^{-}	PO_4^{-}
MS-4-L-CHEM-02	0.2	9.45	6.411	3593	24	391	1149	7241	3647	<60	<60
MS-4-L-CHEM-03	0.0	9.88	12.61	8855	55	623	1820	17087	4926	<60	<60
MS-5-S-CHEM-01	12.7	8.11	21.71	3037	41	1850	16372	33912	11579	2338	<60
MS-5-S-CHEM-02	13.8	8.16	21.34	6540	45	1046	13901	33137	13213	654	<60
MS-5-S-CHEM-03	9.8	8.13	73.78	62460	38	1454	16837	130712	19079	1600	<600
MS-5-L-CHEM-01	9.2	7.72	58.46	23608	68	2571	31340	109554	3316	3484	<600
MS-5-L-CHEM-02	7.7	8.02	77.42	60031	81	2331	21005	148415	2562	1691	<600
MS-5-L-CHEM-03	8.3	7.94	86.76	67960	83	2675	24376	166922	7962	2122	<600
MS-6-S-CHEM-01	2.4	8.89	9.481	5121	20	566	4027	9697	12162	<60	<60
MS-6-S-CHEM-02	3.0	9.11	10.13	6252	26	708	3103	11937	9938	<60	<60
MS-6-S-CHEM-03	2.3	9.04	11.17	7358	30	737	2835	14343	8498	<60	<60
MS-6-L-CHEM-01	1.0	9.56	25.35	21110	98	1247	2314	39596	5288	<60	<60
MS-6-L-CHEM-02	1.0	9.79	24.68	19500	147	1558	2608	38436	5882	<60	<60
MS-6-L-CHEM-03	0.8	9.62	19.46	15688	62	809	2607	29302	6492	<60	<60
LS-E-S-CHEM-01	14.6	8.16	11.5	1495	26	681	10133	14313	12973	2086	<60
LS-E-S-CHEM-02	14.0	8.26	6.266	456	12	228	6385	5244	12036	613	<60
LS-E-S-CHEM-03	13.2	8.21	6.852	496	14	278	7021	5857	13284	818	<60
LS-E-L-CHEM-01	11.7	8.05	19.96	3888	40	1412	15606	30858	13726	2019	<60
LS-E-L-CHEM-02	12.4	8.18	7	933	15	315	6223	7307	9187	2231	<60
LS-E-L-CHEM-03	13.9	8.23	10.71	1210	22	606	10357	12993	14918	1368	<60
LS-W-S-CHEM-01	13.6	8.44	8.501	1112	19	431	8150	7372	14601	2810	<60
LS-W-S-CHEM-02	13.7	8.26	7.842	808	13	326	7066	7528	11676	997	<60
LS-W-S-CHEM-03	13.6	8.21	5.528	526	11	228	4516	5143	6987	903	<60
LS-W-L-CHEM-01	13.4	8.16	13.64	1577	23	906	11995	17919	13953	2477	<60
LS-W-L-CHEM-02	13.3	8.24	9.431	1154	16	458	7788	11062	10037	1128	<60
LS-W-L-CHEM-03	13.8	8.32	11	1255	18	597	9003	12839	11486	1467	<60

Appendix C: Full Statistical Results

Figure C-1. Box-Cox Transformations of simulated crust chemistry data.

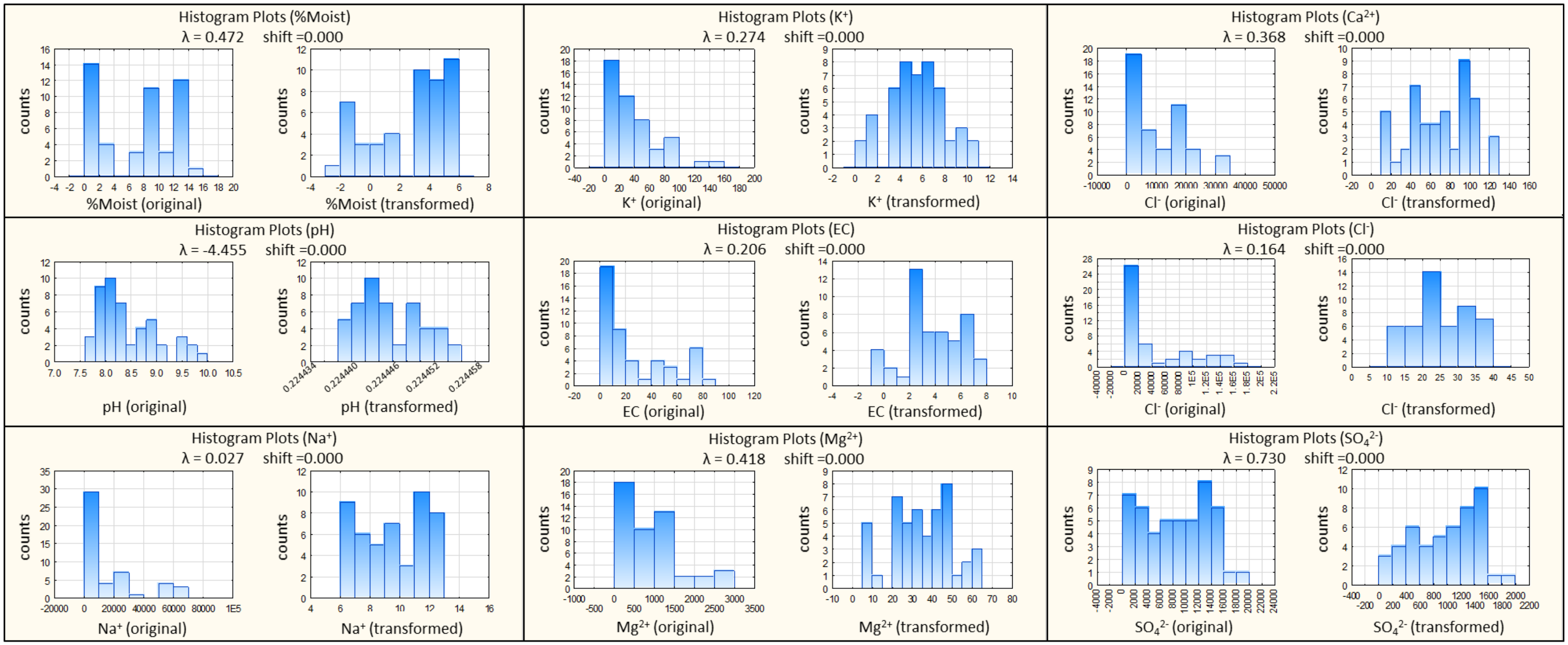

Figure C-2. Analysis of variance based on saltwater-delivery method.

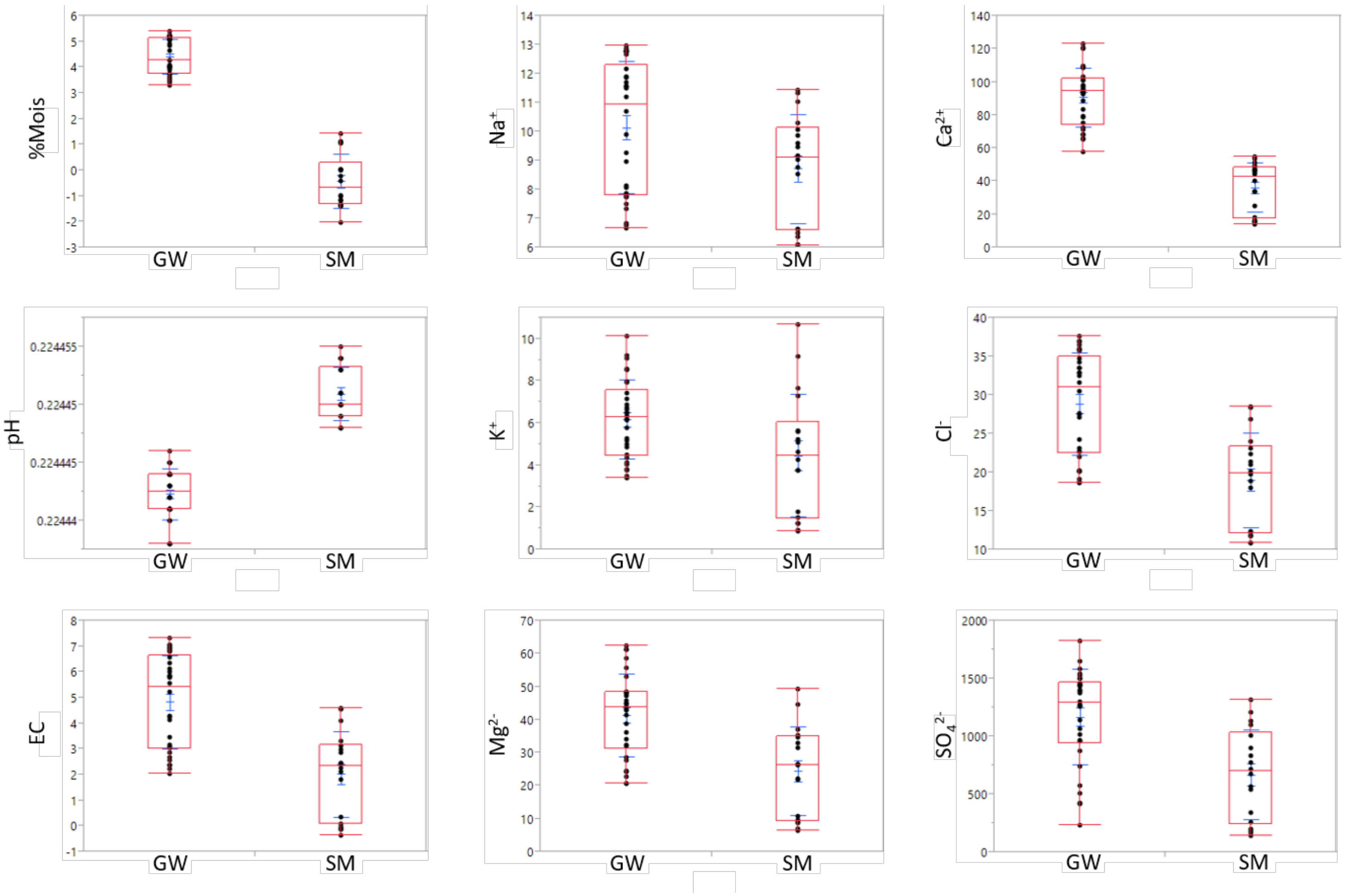

Figure C-3. Analysis of variance based on saltwater-delivery method and direct (D) vs indirect lighting (I).

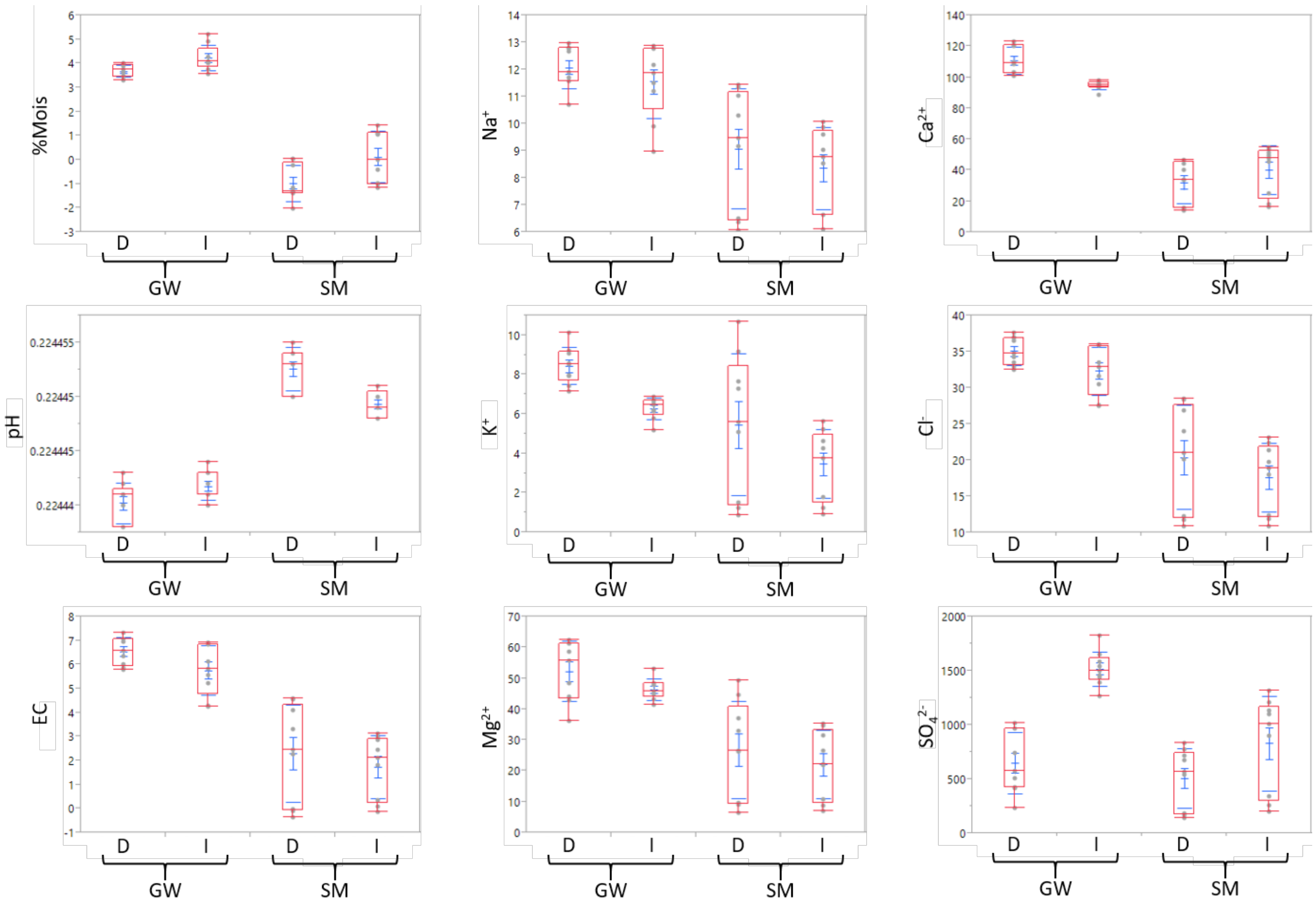

Figure C-4. Analysis of variance based on TDS for tented meter-scale test plots.

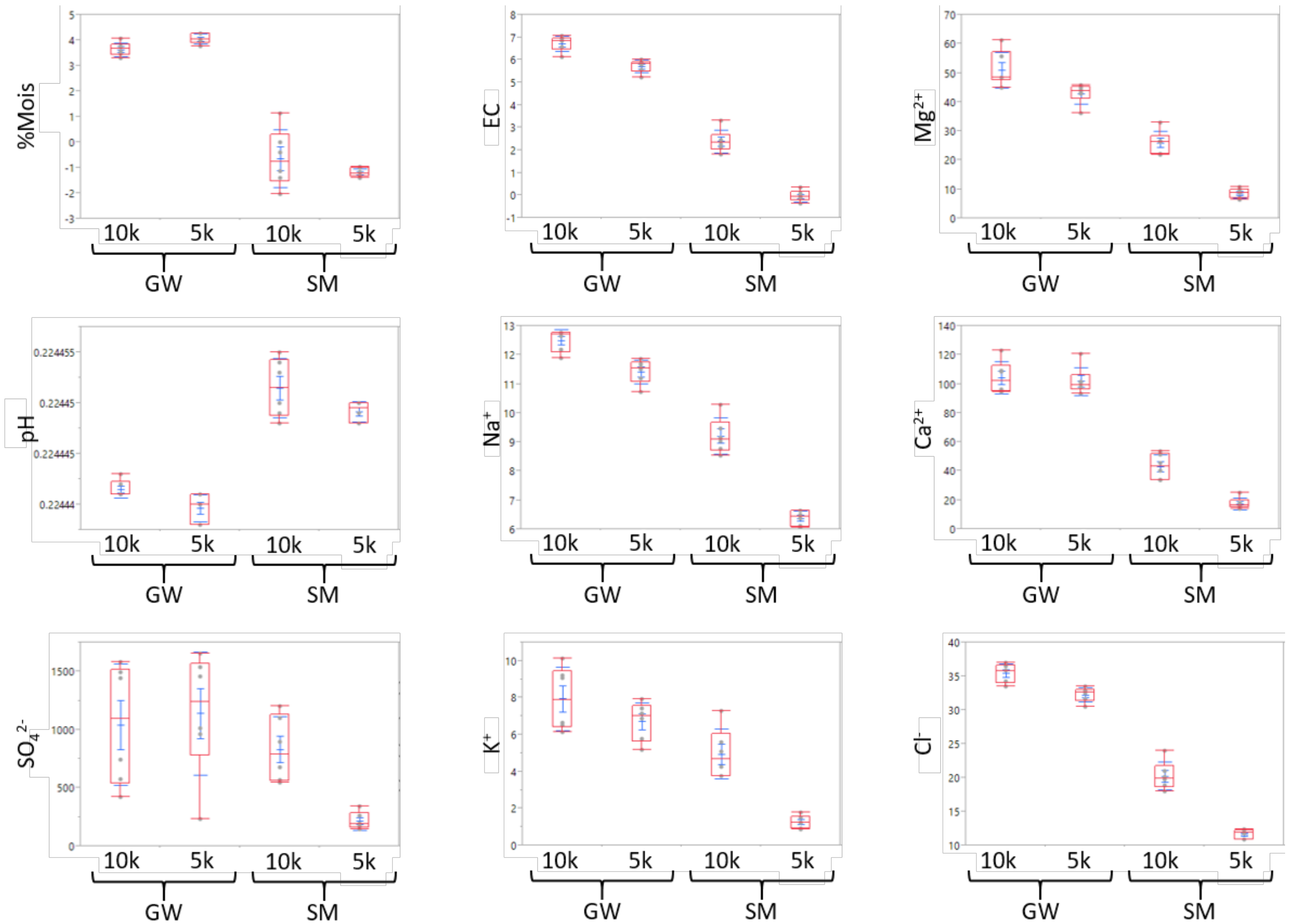

Figure C-5. Box-Cox transformation of physical crust data for large-scale test plot.

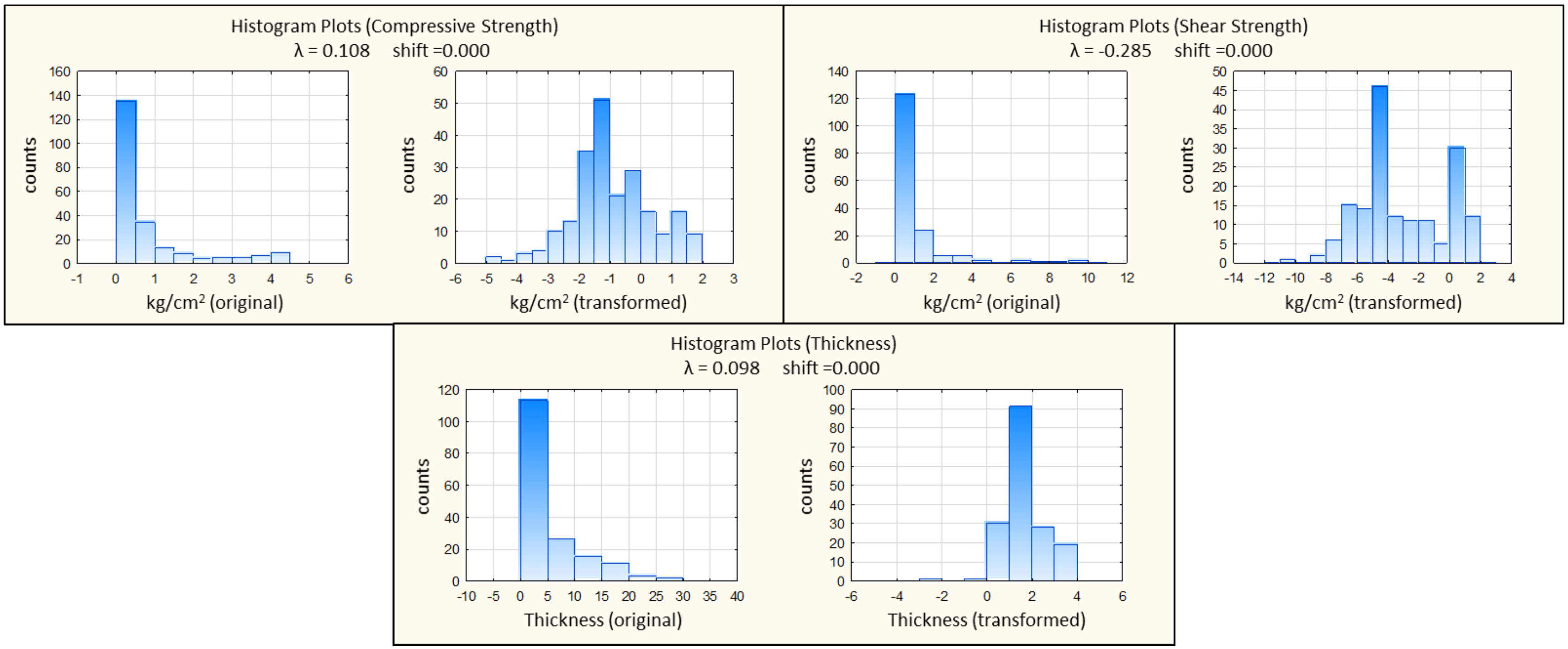

Figure C-6. Analysis of variance of physical crust data for meter-scale test plot based on saltwater-delivery method.

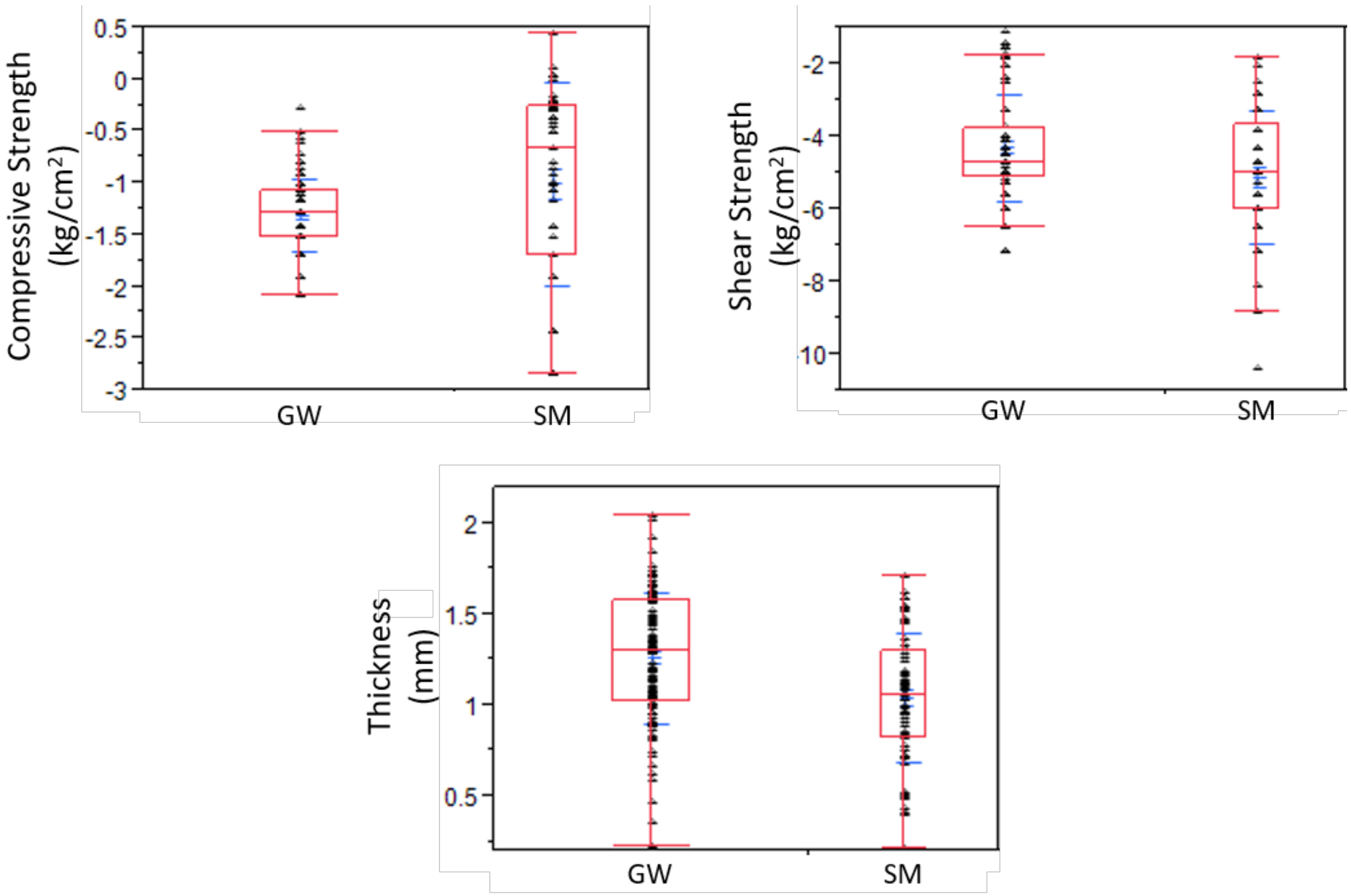

Figure C-7. Analysis of variance of physical crust data for large- and meter-scale test plots based on saltwater-delivery method and direct (D) vs indirect lighting (I).

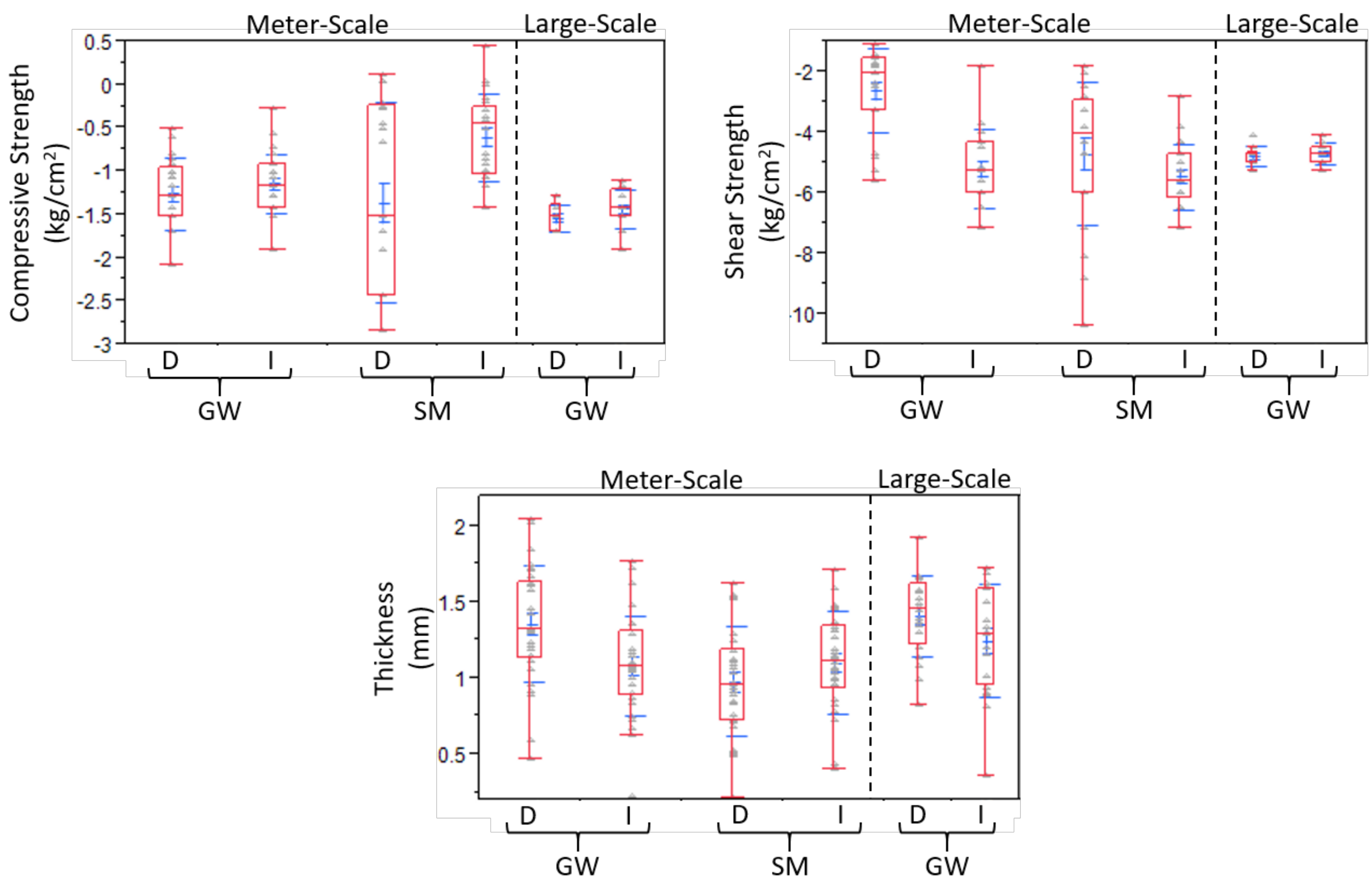

Figure C-8. Analysis of variance of physical crust data for large- and meter-scale test plots based on saltwater-delivery method and TDS.

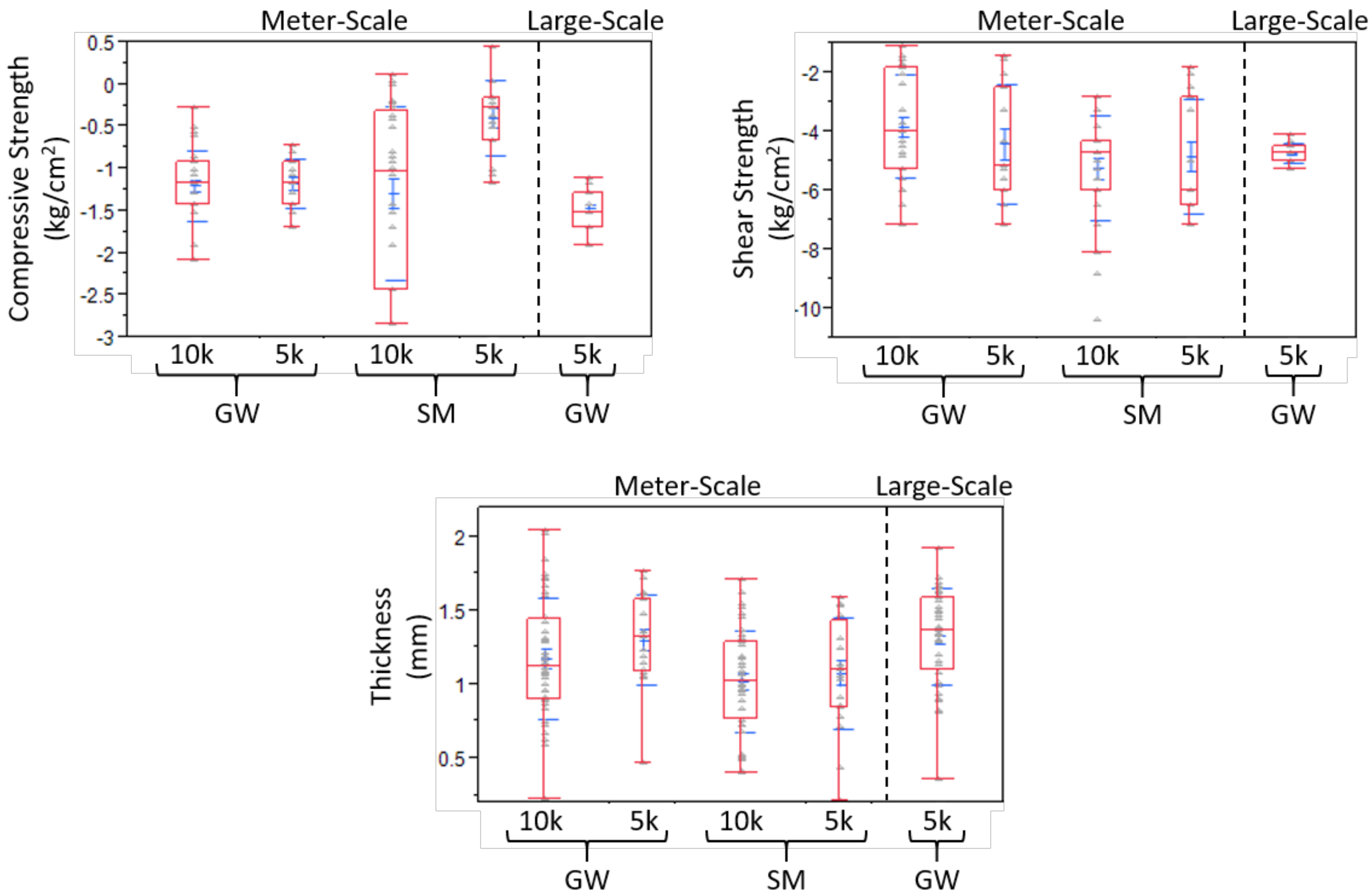

REPORT DOCUMENTATION PAGE

Form Approved OMB No. 0704-0188

1. REPORT DATE *(DD-MM-YYYY)*
August 2019

2. REPORT TYPE
Technical Report/Final

3. DATES COVERED *(From - To)*

4. TITLE AND SUBTITLE
Macroscale Salt-Crust Formation on Indoor Playa-Like Test Plots for Dust-Emission Research Applications: Methodology Assessment

5a. CONTRACT NUMBER

5b. GRANT NUMBER

5c. PROGRAM ELEMENT NUMBER

6. AUTHOR(S)
Matthew F. Bigl, Sandra L. LeGrand, Samuel A. Beal,
Ariana Sopher, and David B. Ringelberg

5d. PROJECT NUMBER

5e. TASK NUMBER

5f. WORK UNIT NUMBER

7. PERFORMING ORGANIZATION NAME(S) AND ADDRESS(ES)
U.S. Army Engineer Research and Development Center (ERDC)
Cold Regions Research and Engineering Laboratory (CRREL)
72 Lyme Road
Hanover, NH 03755-1290

8. PERFORMING ORGANIZATION REPORT NUMBER
ERDC/CRREL TR-19-16

9. SPONSORING / MONITORING AGENCY NAME(S) AND ADDRESS(ES)
Assistant Secretary of the Army for Acquisition, Logistics, and Technology
103 Army Pentagon
Washington, DC 20314-1000

10. SPONSOR/MONITOR'S ACRONYM(S)
ASA(ALT)

11. SPONSOR/MONITOR'S REPORT NUMBER(S)

12. DISTRIBUTION / AVAILABILITY STATEMENT
Approved for public release; distribution is unlimited.

13. SUPPLEMENTARY NOTES
ERDC 6.2 Geospatial Research and Engineering (GRE) ARTEMIS STO-R, funded under WIC 4433FB/U4357514

14. ABSTRACT
Playas (dry lakebeds), which are often used as stable surfaces for landing zones and ground maneuver, can also be prolific sources of dust. Accurate prediction of playa susceptibility to dust emission is essential for military operations in arid regions. The goal of this study was to determine if methodologies originally developed for bench-scale laboratory analyses of surficial salt-crust features common to playas could also be used to create macroscale samples for dust-related research applications in a large-scale indoor testing facility.

Playa salt crust conditions were simulated on six meter-scale plots (2 m × 2 m) and one large-scale plot (7.3 m × 5.5 m) of compacted, well-mixed loamy soil by controlling climatic parameters, the water-delivery mechanism, and surface-soil heating. The resulting simulated-playa surfaces were characterized for developed crust thickness, compressive and shear strength, chemical composition, and dust-emission potential. Resultant crust attributes varied; however, all methods tested developed simulated playas with physical conditions that were comparable to real-world analogues. Although chemical composition was not evaluated in our real-world comparison, we found that our water delivery method had a statistically significant effect on the chemical attributes of the simulated crusts.

15. SUBJECT TERMS
Dust; Dust emission; Dust storms; Engineered environment; Groundwater processes; Playas; Salt Crust; Vehicles, Military

16. SECURITY CLASSIFICATION OF: a. REPORT	b. ABSTRACT	c. THIS PAGE	17. LIMITATION OF ABSTRACT	18. NUMBER OF PAGES	19a. NAME OF RESPONSIBLE PERSON / 19b. TELEPHONE NUMBER *(include area code)*
Unclassified	Unclassified	Unclassified	SAR	72	